

# Electron-Ion Recombination Rate Coefficients and Photoionization Cross Sections for S XIV and S XV for X-ray and UV modeling

Sultana N. Nahar

Department of Astronomy, The Ohio State University, Columbus, OH 43210, USA

E-mail: [nahar@astronomy.ohio-state.edu](mailto:nahar@astronomy.ohio-state.edu)

**Abstract.** The inverse processes of photoionization and electron-ion recombination of ( $h\nu + \text{S XIV} \rightleftharpoons \text{S XV} + e$ ) and ( $h\nu + \text{S XV} \rightleftharpoons \text{S XVI} + e$ ) are studied in detail using ab initio unified method that provides self-consistent sets of results for these processes. Results are presented for large number of fine structure levels where  $n \leq 10$  and  $0 \leq l \leq 9$ ; 98 levels for Li-like S XIV with  $1/2 \leq J \leq 17/2$  and 188 levels for He-like S XV with  $0 \leq J \leq 10$ . Photoionization cross section,  $\sigma_{PI}$ , of the levels of both S XIV and S XV decay smoothly in the lower region. However, narrow and high peak autoionizing Rydberg series of resonances belonging to various excited core levels appear in the high energy region and enhance the background cross section of the excited levels. The resonance series of  $n=2$  core levels dominate while they become weaker with higher  $n$ . The prominent feature is the enhancement of the background cross section at  $n=2$  core thresholds due to K-shell ionization leaving the ion in excited 2p states.  $\sigma_{PI}$  also show wide PEC (photo-excitation-of-core) resonances at the photon energies that equal to the core excitation energies. Level-specific photoionization cross sections,  $\sigma_{PI}(nSLJ)$ , and recombination rate coefficients,  $\alpha_{RC}(nSLJ)$ , are obtained for the first time for these ions. Currently available results correspond to photoionization for LS terms with missing features and to only total recombination rate coefficients. Present  $\alpha_{RC}(nSLJ)$  incorporates both the radiative recombination (RR) and dielectronic recombination (DR), and show a 'bump' or 'shoulder' in the high temperature region due to DR dominance. The total unified recombination rate coefficients show good agreement with the available RR and DR rates. Recombination rates over photoelectron energy are presented for astrophysical and laboratory plasma applications. Total recombination rates for H-like S XVI are given for completeness. The results should be accurate within 10-15% based on the unified method that includes important atomic effects such as radiation damping, channel couplings, interference of DR and RR, and relativistic fine structure effects. The comprehensive datasets are applicable for various models such as for ionization balance and recombination-cascade for UV and X-ray lines.

PACS numbers: 32.30.-r; 32.30.Jc, 32.30.Rj; 32.80.Fb

*Keywords:* Photoionization; Electron-ion recombination; UV and X-rays; S XIV, S XV, S XVI

## 1. Introduction

H-, He-like and Li-like sulfur (S XVI, S XV, S XIV) are prevalent in high-temperature astrophysical (e.g. solar corona) and laboratory (e.g. tokomaks) plasmas. However, X-ray spectra taken by space observatories, such as Chandra, XMM-Newton show existence of these ions in the cooler photoionized plasmas (e.g. Liedahl & Paerls 1996, Reeves et al. 2002, Brinkman et al. 2002, Paerls et al. 2000, Marshall et al. 2002). Spectral lines of these ions provide information of various physical conditions and processes in the objects. For example, ASCA observation of H-like S emission in the X-ray binary star system Cygnus X-3 was explained by Liedahl & Paerls (1996) of excitation by recombination in a tenuous X-ray photoionized plasmas. In a later observation of Cygnus X-3, but using Chandra, Paerls et al. (2000) provide for He-like S XV the diagnostic quantity,  $f/(r+i)$ , for recombination to be 1.0. For a helium like ion, (f,r,i) correspond to  $K\alpha$  X-ray lines, w (r-resonant), x (f-forbidden), y (i-intercombination), z (f-forbidden) and involve transitions between  $n = 2$  and  $n=1$  levels. They provide information of temperature, density, and ionization state of the plasma (e.g. Oelgoetz & Pradhan 2001, 2004). Brinkman et al. (2002) explained their observation of S XV and S XVI emission lines alongwith some other elements in the bright spot near NGC 1069 to be formed from recombination or radiative cascade following photoionization, and radiative decay following photoexcitation. The ionization balance in the source requires knowledge of ionization and electron-ion recombination rates for the ionization stage of He-like as well as Li-like and H-like stages. Emission lines in general contain a component due to electron-ion recombination, especially in transient plasmas out of ionization equilibrium. To model the recombination component, recombination-cascade coefficients are computed from level-specific recombination rate coefficients for a large number of excited levels, as presented in this report. However existng photoionization cross sections and recombination rates are from simpler considerations that do not include important effects and are incomplete. Earlier calculations for photoionization cross sections for these ions were carried out under the Opacity Project (OP) by Fernley et al. (1987) for He-like ions and by Peach et al. (1988) for Li-like ions. They were computed in the non-relativistic LS coupling and using much smaller wavefunctions than the present ones. There are no level-specific phtooionization cross sections for fine structure levels with autoionizing resonances or level-sepcific recombination rates that include both the radiative and dielectronic recombination rates for these sulfur ions. Existing recombination rates available are for total radiative recombination from central field approximation (e.g Verner & Ferland 1996), and for total dielectronic recombination using isolated resonance approximation (e.g. Romanik 1988). The aim of the present work is to provide accurate quantities for photoionization and recombination for accurate astrophysical modeling.

The present results for S XIV and S XV should be useful for spectral analysis of X-ray observations from Chandra X-ray Observatory and XMM-Newton, and UV observatories, such as Far Ultraviolet Explorer (FUSE), the Solar and Heliospheric

Observatory (SOHO) etc. The data are presented at all energies and temperatures prevalent in sources such as stars, nebulae, active galactic nuclei, supernova remnants, hot stellar coronae etc.

## 2. Theory

Photoionization and electron-ion recombination are inverse to each other which for an ion  $X^+$  can be expressed as,

$$e + X^{++} \rightleftharpoons h\nu + X^+, \quad (1)$$

where right arrow indicates the direct or radiative recombination (RR) and the left arrow indicates photoionization. The processes may go through in two steps,

$$e + X^{++} \rightleftharpoons (X^+)^{**} \rightleftharpoons \begin{cases} a) e + X^{++}(AI) \\ b) h\nu + X^+(DR) \end{cases}, \quad (2)$$

where the intermediate doubly excited state is an autoionizing state. This state may lead either to autoionization (AI) where the electron goes free or to dielectronic recombination (DR) via emission of a photon (radiation damping). The state introduces a resonance in photoionization and recombination cross sections. RR and DR are inseparable in nature although one may dominate the other at different temperatures and energies. The unified method subsumes both the RR and DR processes and considers photoionization from and recombination into the infinity of (e + ion) levels. It is an ab initio method implemented in the close coupling (CC) approximation and R-matrix method (Nahar & Pradhan 1992, 1994) as briefly outlined below.

The CC approximation treats the atomic system of an ion interacting with another electron as (N+1)-electron system where the ion has  $N$  number of electrons and is termed as the target. The (N+1)th electron can be bound to the ion or in the continuum depending on its negative or positive energy. The total (N+1)-electron wavefunction,  $\Psi(E)$ , at symmetry  $J\pi$  is represented by an expansion of target eigenfunctions,  $\chi_i$ , as:

$$\Psi(\text{ion} + e; E) = A \sum_i \chi_i(\text{ion})\theta_i + \sum_j c_j \Phi_j(\text{ion} + e), \quad (3)$$

where the target is in a specific level  $J_i\pi_i$ .  $\theta_i$  is the wavefunction of the (N+1)-th interacting electron in a channel,  $S_i L_i(J_i)\pi_i k_i^2 \ell_i(J\pi)$  and  $k_i^2$  is its kinetic energy. The channel is called open or closed depending on positive or negative energy ( $k_i^2$ ). The autoionizing resonances result from the couplings of open and closed channels. The  $\Phi_j$ 's are correlation functions of the (N+1)-electron system and account for short range correlations and orthogonality between continuum and bound orbitals.

The present calculations implement relativistic Briet-Pauli R-matrix (BPRM) method as adopted under the Iron Project (Hummer et al. 1993) where the Hamiltonian is given by

$$H_{N+1}^{\text{BP}} = H_{N+1}^{\text{NR}} + H_{N+1}^{\text{mass}} + H_{N+1}^{\text{Dar}} + H_{N+1}^{\text{so}}. \quad (4)$$

The first term,  $H_{N+1}^{NR}$ , is the nonrelativistic Hamiltonian,

$$H_{N+1}^{NR} = \sum_{i=1}^{N+1} \left\{ -\nabla_i^2 - \frac{2Z}{r_i} + \sum_{j>i}^{N+1} \frac{2}{r_{ij}} \right\}, \quad (5)$$

and the additional one-body terms represent the mass correction,  $H^{\text{mass}} = -\frac{\alpha^2}{4} \sum_i p_i^4$ , Darwin,  $H^{\text{Dar}} = \frac{Z\alpha^2}{4} \sum_i \nabla^2 \left( \frac{1}{r_i} \right)$  and spin-orbit interaction,  $H^{\text{so}} = Z\alpha^2 \sum_i \frac{1}{r_i^3} \mathbf{l}_i \cdot \mathbf{s}_i$ . The spin-orbit term splits the  $LS$  term into fine structure components. The set of  $SL\pi$  is recoupled for  $J\pi$  levels of (e + ion)-system which is followed by diagonalization of the Hamiltonian,  $H_{N+1}^{BP} \Psi = E\Psi$ . The solutions are continuum  $\Psi_F$  or bound  $\Psi_B$  states with positive energy ( $E = k^2 \geq 0$ ) or negative energy ( $E < 0$ ) and are used in the transition matrix elements.

The reduced matrix element for the bound-free transition is obtained as  $\langle \Psi_B || \mathbf{D} || \Psi_F \rangle$  where  $\mathbf{D} = \sum_i r_i$  is the dipole operator, the sum is the number of electrons. The dipole line strength,  $\mathbf{S} = | \langle \Psi_B || \mathbf{D} || \Psi_F \rangle |^2$ , gives the photoionization cross section,  $\sigma_{PI} = [4\pi^2/(3g_i c)] \omega \mathbf{S}$ , where  $g_i$  is the statistical weight factor of the initial bound state and  $\omega$  is the photon frequency.

Radiation damping of resonances is significant for S XIV and S XV. Radiative decay rates ( $A_r$ ) of sulfur ions are large for transitions,  $2p(^2P_{3/2,1/2}^o) \rightarrow 1s(^2S_{1/2})$  with H-like core and  $1s2p(^1P_1^o) \rightarrow 1s^2(^1S_0)$  with He-like core. They compete with autoionization rates, typically  $A_a \sim 10^{12} - 10^{14} \text{ sec}^{-1}$  and cause autoionizing resonances to damp radiatively to a significant extent. The radiation damping effect is included using a resonance fitting procedure (Sakimoto et al. 1990, Pradhan & Zhang 1997, Zhanget al 1999). All resonances, up to effective quantum number  $\nu \leq 10$ , have been damped. Resonances beyond  $\nu > 10$  are treated with DR theory discussed below.

The electron-ion recombination cross section  $\sigma_{RC}$  can be obtained from photoionization cross sections  $\sigma_{PI}$  using principle of detailed balance as, in Rydberg units,

$$\sigma_{RC}(\epsilon) = \frac{\alpha^2 g_i (\epsilon + I)^2}{4 g_j \epsilon} \sigma_{PI}, \quad (6)$$

which is known as the Milne relation. Here  $\alpha$  is the fine structure constant,  $\epsilon$  is the photoelectron energy,  $g_j$  is the statistical weight factor of the recombined ion and  $I$  is the ionization potential.  $\sigma_{RC}$  computed from  $\sigma_{PI}$  with sufficiently large number of energies to delineate the non-resonant background and the autoionizing resonances represents both RR and DR processes. For the recombining ion in its ground state,  $\sigma_{PI}$  corresponds to partial photoionization cross sections, leaving the ion in the ground state. Recombination rate coefficients,  $\alpha_R(nSLJ)$ , of individual recombined levels are obtained by convolving  $\sigma_{RC}$  over Maxwellian electron distribution  $f(v) = \frac{4}{\sqrt{\pi}} \left( \frac{m}{2kT} \right)^{3/2} v^2 e^{-\frac{mv^2}{2kT}}$  at a given temperature as,

$$\alpha_R(i, T) = \int_0^\infty v f(v) \sigma_{RC}(i) dv, \quad (7)$$

where  $i = nSLJ$ . The sum of these individual rates  $\sum_i \alpha_R(i, T)$  provides the contribution to the total recombination rate coefficient,  $\alpha_R$  and the total recombination cross sections,  $\sigma_{RC}$ .

Total recombination rates of the electron-ion system correspond to contributions from infinite number of recombined states. In unified method, the recombined states are divided into two groups: group (A) states  $n \leq n_o$  with all possible fine structure  $J\pi$  symmetries and group (B) states with  $n_o < n \leq \infty$ , with  $n_o \sim 10$ . The recombination rates coefficients of group (A) states are obtained from the photoionization cross sections as described above.

Group (B) levels,  $n_o < n \leq \infty$ , are treated through quantum defect theory of DR within the close coupling approximation (Bell & Seaton 1985, Nahar & Pradhan 1992, 1994). This small energy region is dominated by DR via the high- $n$  resonances converging on to the thresholds in the core ion. The background contribution of these levels is negligible except at very low temperature. The DR contributions from these levels are obtained from the collision strengths,  $\Omega(\text{DR})$ , using radiation damping theory as:

$$\Omega(\text{DR}) = \sum_{SL\pi} \sum_n (1/2)(2S+1)(2L+1) P_n^{SL\pi}(\text{DR}). \quad (8)$$

where the DR probability  $P_n^{SL\pi}$  in entrance channel  $n$  is,  $P_n^{SL\pi}(\text{DR}) = (\mathbf{1} - \mathbf{S}_{ee}^\dagger \mathbf{S}_{ee})_n$ ,  $\mathbf{S}_{ee}$  is the matrix for electron scattering *including* radiation damping. The cross section,  $\sigma_{RC}$  in Mb, and collision strength,  $\Omega_{RC}$ , for recombination are related as

$$\sigma_{RC}(i \rightarrow j)(\text{Mb}) = \pi \Omega_{RC}(i, j) / (g_i k_i^2) (a_o^2 / 1. \times 10^{-18}), \quad (9)$$

where  $k_i^2$  is in Rydbergs. For numerical stability,  $\Omega_{RC}$  is preferable to  $\sigma_{RC}$  for calculation of recombination rate coefficient since  $\sigma_{RC}$  diverges at zero-photoelectron energy. Background photoionization cross sections for the high- $n$  group (B) levels are computed hydrogenically, and the corresponding contribution to  $\alpha_R$  is referred to as the “high- $n$  top-up” (Nahar 1996).

The total recombination cross sections  $\sigma_{RC}$ , summed from contributions of group A and B states, provides important information on dielectronic satellite lines (Nahar & Pradhan 2006). It is also used to calculate the photorecombination rates  $\alpha_{RC}(E)$  with photoelectron energy  $E$  which can be measured in laboratory set-ups. The velocity ( $v$ ) or energy dependent photorecombination rate can be obtained as,

$$\alpha_{RC}(E) = v \sigma_{RC}(E), \quad (10)$$

The measurable feature is the resonant part of  $\alpha_{RC}(E)$  convolved with the monochromatic bandwidth of the experimental beam in synchrotron facilities such as the Test Storage Ring in Heidelberg (e.g. Pradhan et al. 2001).

### 3. Computation

The calculations for photoionization and electron-ion recombination involve number of stages, largely using R-matrix package of codes (Berrington et al. 1987, 1995) and their

**Table 1.** Target levels and energies in the eigenfunction expansions of S XV and S XVI, and dipole allowed transitions to the ground levels. Target S XV was optimized with correlation configurations,  $2s^2$ ,  $2p^2$ ,  $3s^2$ ,  $3p^2$ ,  $3d^2$ ,  $2s2p$ ,  $2s3s$ ,  $2s3p$ ,  $2s3d$ ,  $2s4s$ ,  $2s4p$ ,  $2p3s$ ,  $2p3p$ ,  $2p3d$ ,  $2p4s$ ,  $2p4p$  and the orbital scaling parameter  $\lambda$  with values 1.1(1s), 0.991(2s), 1(2p), 1(3s), 1(3p), 1(3d), 1(4s), 1(4p). For S XVI, there is no correlation and  $\lambda=1$  for all orbitals.

S XV			S XVI	
level		E(Ry)	level	E(Ry)
1	$1s^2\ ^1S_0$	0.0	$1s\ ^2S_{1/2}$	0.0
2	$1s2s\ ^3S_1$	178.62726	$2p\ ^2P_{1/2}^o$	192.544
3	$1s2p\ ^3P_0^o$	179.83231	$2s\ ^2S_{1/2}$	192.552
4	$1s2p\ ^3P_1^o$	179.86153	$2p\ ^2P_{3/2}^o$	192.765
5	$1s2s\ ^1S_0$	179.93399	$3p\ ^2P_{1/2}^o$	228.276
6	$1s2p\ ^3P_2^o$	179.98047	$3s\ ^2S_{1/2}$	228.279
7	$1s2p\ ^1P_1^o$	180.85266	$3d\ ^2D_{3/2}$	228.342
8	$1s3s\ ^3S_1$	211.35166	$3p\ ^2P_{3/2}^o$	228.342
9	$1s3p\ ^3P_0^o$	211.68343	$3d\ ^2D_{5/2}$	228.363
10	$1s3p\ ^3P_1^o$	211.69236	$4p\ ^2P_{1/2}^o$	240.774
11	$1s3s\ ^1S_0$	211.69725	$4s\ ^2S_{1/2}$	240.775
12	$1s3p\ ^3P_2^o$	211.72770	$4d\ ^2D_{3/2}$	240.801
13	$1s3d\ ^3D_1$	211.91161	$4p\ ^2P_{3/2}^o$	240.801
14	$1s3d\ ^3D_2$	211.91192	$4f\ ^2F_{5/2}^o$	240.810
15	$1s3d\ ^3D_3$	211.92578	$4d\ ^2D_{5/2}$	240.810
16	$1s3d\ ^1D_2$	211.93516	$4f\ ^2F_{7/2}^o$	240.815
17	$1s3p\ ^1P_1^o$	211.96451		

Radiative decay rates to ground level,  $1s^2(^1S_0)$  for S XV &  $1s(^2S_{1/2})$  for S XVI, from various excited levels

S XV		S XVI	
Level	$A_{fi}(s^{-1})$	Level	$A_{fi}(s^{-1})$
$1s2p(^3P_1^o)$	5.21E+11	$2p(^2P_{1/2}^o)$	4.09E+13
$1s2p(^1P_1^o)$	6.64E+13	$2p(^2P_{3/2}^o)$	4.09E+13
$1s3p(^3P_1^o)$	1.59E+11	$3p(^2P_{1/2}^o)$	1.06E+13
$1s3p(^1P_1^o)$	1.89E+13	$3p(^2P_{3/2}^o)$	1.08E+13
		$4p(^2P_{1/2}^o)$	4.12E+12
		$4p(^2P_{3/2}^o)$	4.22E+12

extensions as described below.

The first step, before start of R-matrix codes, is to obtain the orbital wavefunctions of the target or the core. They are obtained from configuration interaction atomic structure calculations using the code SUPERSTRUCTURE (Eissner et al. 1974).

The wavefunction expansion for the Li-like S XIV contains 17 fine structure levels of the *spectroscopic* configurations  $1s^2$ ,  $1s2s$ ,  $1s2p$ ,  $1s3s$ ,  $1s3p$ , and  $1s3d$  of the target core S XV. The levels and their energies are given in Table 1. The set of *correlation* configurations and the Thomas-Fermi scaling parameters for each orbital in the atomic structure calculations are also given in Table 1.

The wavefunction expansion for S XV contains 16 fine structure levels of S XVI of configurations  $1s$ ,  $2s$ ,  $2p$ ,  $3s$ ,  $3p$ ,  $3d$ ,  $4s$ ,  $4p$ ,  $4d$  and  $4f$ . The levels and their energies are given also in Table 1. For both targets, S XV and S XVI, the calculated energies agree with observed values in less than 1%.

The computations with R-matrix codes including relativistic effects through Breit-Pauli approximation (BPRM) (Berrington et al. 1987, 1995) start with the input of

these orbital wavefunctions from SUPERSTRUCTURE. The first stage, STG1, includes the second term of the wavefunction in Eq. (3) representing bound state correlation functions. For S XIV all possible  $(N+1)$ -particle configurations with 0 to maximum orbital occupancies of  $2s^2$ ,  $2p^2$ ,  $3s^2$ ,  $3p^2$ ,  $3d^2$ ,  $4s$  and  $4p$  are included. The radial integrals for the partial wave expansion are specified for  $0 \leq \ell \leq 9$ , with a R-matrix basis set of 40 continuum functions. Computations are carried out for all angular momenta,  $0 \leq L \leq 11$ . For S XV, the bound state correlation functions included all possible configurations from 0 to maximum orbital occupancies of  $1s^2$ ,  $2s^2$ ,  $2p^2$ ,  $3s^2$ ,  $3p^2$ ,  $3d^2$ ,  $4s^2$ ,  $4p^2$ ,  $4d$  and  $4f$ . The partial wave expansion includes all orbitals  $0 \leq \ell \leq 9$ , with a R-matrix basis set of 30 continuum functions. Computations are carried out for all angular momenta,  $0 \leq L \leq 14$ . Next stages of computations proceeded similar to earlier BPRM calculations, such as those for Ni XXVI and Ni XXVII (Nahar 2005).

Both the partial and the total photoionization cross sections are obtained for all bound levels using the extensions (Nahar & Pradhan 1994, Zhang et al. 1999) of the BPRM codes that include the relativistic Breit-Pauli effects (Scott & Burke 1980, Scott & Taylor 1982). The energy levels are obtained from STGB and are identified using the code PRCPID (Nahar & Pradhan 2000). Radiation damping of resonances up to  $n = 10$  are included using the extended codes STGF and STGBF (Nahar & Pradhan 1994, Zhang et al. 1999). The narrow resonances of these ions were delineated at a very fine energy mesh. The program PBPRAD extends the total photoionization cross sections in the high energy region beyond the highest threshold in target ion by a ‘tail’ using a fitting formula,  $\sigma_{PI}^o(E^o/E)^m$ , where  $E^o$  is the last tabulated energy beyond the resonances, that is, at an energy beyond the highest target threshold and  $-1 \geq m \geq -3$ , as described in Nahar & Pradhan (1994).  $m = -3$  for Kramers fit at very high energies. The DR collision strengths for the narrow and dense resonances in the energy region,  $\nu_o < \nu \leq \infty$ , below each target excited threshold were obtained using STGFDR. The radiative decay rates for the allowed excited thresholds used for  $\Omega(DR)$  are given in Table 1.

Recombination cross sections,  $\sigma_{RC}(i)$ , for various bound levels  $i \equiv n(\text{SLJ})$  of the recombined (e + ion) system were obtained from partial photoionization cross sections  $\sigma_{PI}(i, g)$  using the program RECXS. It sums up the level specific rates and adds the resonant contributions of high- $n$  ( $\nu_o \leq \nu \leq \infty$ ) DR for the total recombination rates. As a check on the numerical calculations, the total recombination rate coefficients,  $\alpha_R$ , are also calculated from the total recombination collision strength,  $\Omega_{RC}$ . The two sets of numerical values agreed within a few percent.

#### 4. Results and Discussions

Photoionization and electron-ion recombination of (S XIV +  $h\nu \rightleftharpoons$  S XV + e), (S XV +  $h\nu \rightleftharpoons$  S XVI + e) are studied in detail. Photoionization includes both the *total* and the *partial*. The *total* refers to photoionization when the ionized residual ion can be in the ground or in an excited state and the *partial* refers to ionization only into the ground

state. The present self-consistent set of results include photoionization cross sections and recombination cross sections and rate coefficients for fine structure levels up to  $n \leq 10$  and  $l \leq 9$ . Various features of these processes are discussed in the subsections below.

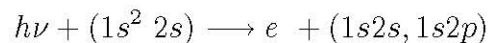
#### 4.1. S XIV

A total of 98 bound fine structure levels of total angular momenta  $1/2 \leq J \leq 17/2$  are obtained for Li-like S XIV with  $n \leq 10$ ,  $0 \leq l \leq 9$ ,  $0 \leq L \leq 11$  (Nahar 2002). The earlier results (Nahar 2002) are for oscillator strengths for radiative transitions obtained using the same BPRM approximation and same wavefunction, and hence are consistent with the present results for photoionization and recombination.

*4.1.1. Photoionization* The *total* photoionization cross sections ( $\sigma_{PI}$ ), which include contributions from all channels for ionization into the ground and various excited states of the residual ion, are presented for all 98 fine structure levels of S XIV. *Partial* photoionization are also presented for all 98 fine structure bound levels. Important characteristics in  $\sigma_{PI}$  are illustrated below.

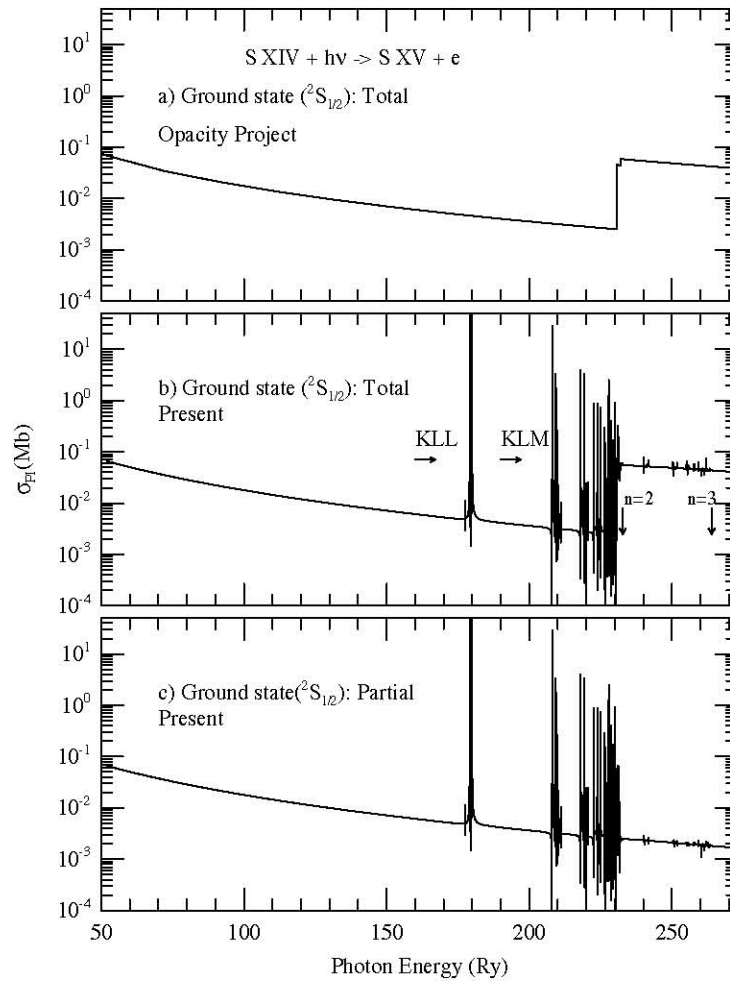
Photoionization cross section of the ground level is needed for ionization fractions and other applications. Figure 1 presents  $\sigma_{PI}$  for both total (panel b) and partial (panel c) photoionization of the ground level  $1s^2 2s^2 S_{1/2}$  of S XIV and compares with the total cross section (panel a) from the OP (Peach et al. 1988). The smooth decay of the cross section of the ground level over a wide energy range is typical for a few electron system. The resonances in  $\sigma_{PI}$  are due to doubly excited autoionizing states  $1snl\nu l'$  of various Rydberg series converging on to the  $n = 2, 3$  levels of the core ion.  $\nu$  is the effective quantum number for an autoionizing state. The resonances start to appear in the high energy region because of core threshold lying in the high energy region. The first resonance complexes are the well known KLL, KLM, etc. complexes belonging to  $n=2$  core thresholds. KLL denotes the series  $1s2l2l$ , KLM denotes  $1s2l3l'$  etc. KLL complex, for example, consists of 22 possible resonances seen as dielectronic satellite lines (e.g. Nahar & Pradhan 2006).

The total and partial cross sections are identical below the first excited level of the residual ion. However, the total  $\sigma_{PI}$  is enhanced beyond  $n=2$  thresholds by the added contributions from excited channels in comparison to the partial cross sections where they are not added. The enhancement at the excited  $n=2$  thresholds is due to the K-shell photoionization:



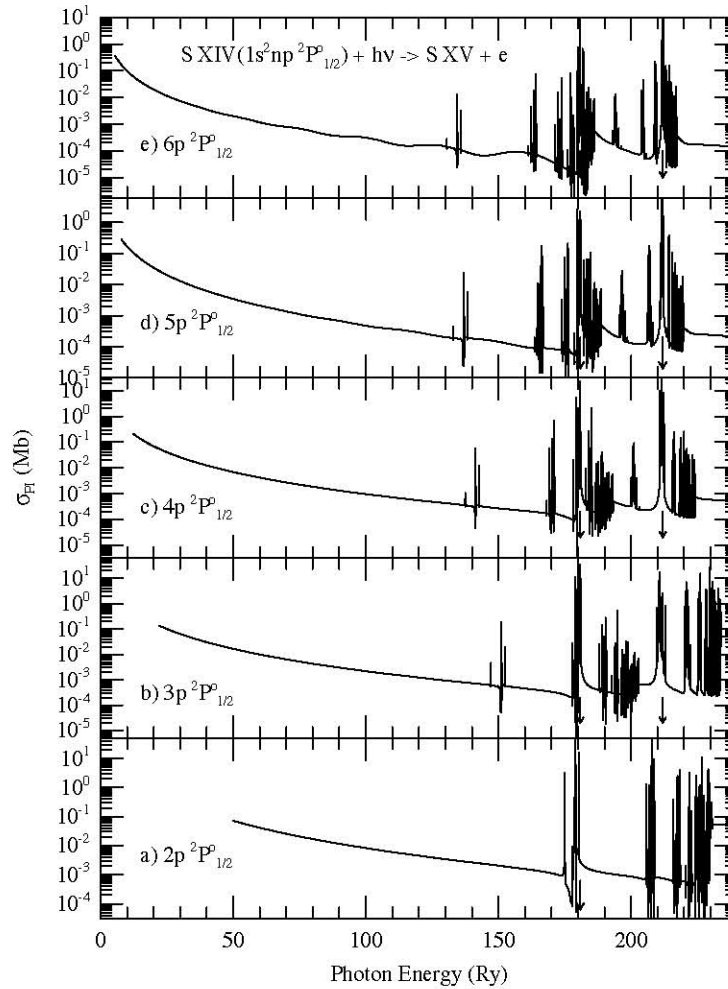
which is at about 232 Ry (sum of ionization energy 51.963 Ry and excitation energy 179.86 Ry for core transition  $1s^2 {}^1S_0 - 1s2p {}^1P_1^o$ ). This inner-shell edge plays an important role in X-ray photoionization models. However, the OP cross sections do not include these resonances. The OP data also do not include partial cross sections needed for cascade matrix, recombination cross sections etc.





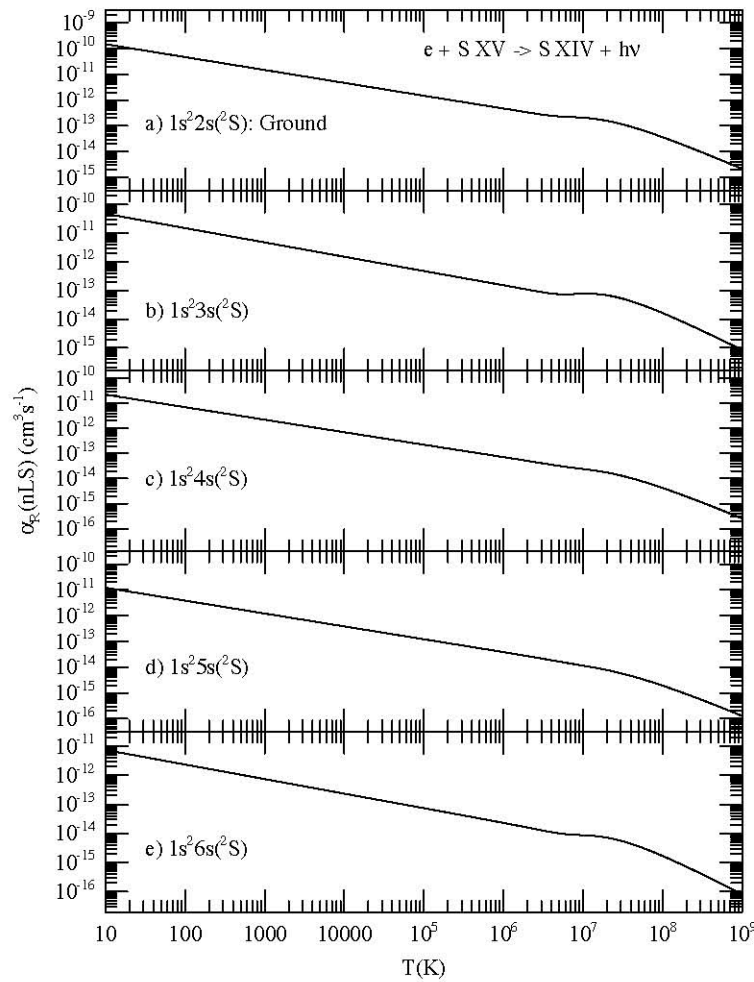
**Figure 1.** *Total* (a - Opacity Project, b - present) and *partial* (c) photoionization cross sections of the ground level  $1s^2 2s ({}^2S_{1/2})$  of S XIV. The enhancement in the total  $\sigma_{PI}$  around  $n = 2$  thresholds ( $\sim 232$  Ry) in (a,b) is due to K-shell ionization ( $h\nu + 1s^2 2l \rightarrow 1s 2l + e$ ). The partial cross section (c) does not show it since ionization into the excited core are not included. The OP cross sections (a) (Peach et al 1988) do not include the resonances.

Figure 2 presents total  $\sigma_{PI}$  of excited Rydberg series of levels  $1s^2 np ({}^2P_{1/2}^o)$ ,  $2 \leq n \leq 6$  of S XIV illustrating the resonant structures at higher energies, especially the photoexcitation-of-core (PEC) resonances. Contrary to hydrogenic decay of the excited state cross sections, PEC resonances enhance the background. These resonances are manifested by dipole transitions from the ground level in the core ion and appear at the excited thresholds of transitions. At photon energies that equal to core excitation energies, the core goes through the allowed  $\Delta J=0-1$  transitions while the



**Figure 2.** Total photoionization cross sections of the excited Rydberg series of levels,  $1s^2 np(^2P_{1/2}^o)$  with  $2 \leq n \leq 6$ , of S XIV illustrating the prominent PEC (*photoexcitation-of-core*) resonances (pointed by arrows) at about 180 Ry due to core excitation to  $n=2$  levels,  $1s^2 \ ^1S_0 - 1s2p \ ^3P_1^o, \ ^1P_1^o$ , and at about 212 Ry to  $n=3$  levels,  $1s^2 \ ^1S_0 - 1s3p \ ^3P_1^o, \ ^1P_1^o$ .

outer electron remains a ‘spectator’ in a doubly-excited resonant state. The state decays via autoionization into the ground level of the core. PEC resonances can be seen in Fig. 2 (pointed by arrows in the figure), at about 180 Ry for  $n=2$  thresholds  $1s2p \ ^3P_1^o, \ ^1P_1^o$  and at about 212 Ry of  $n=3$  thresholds  $1s3p \ ^3P_1^o, \ ^1P_1^o$ . PEC resonances are more enhanced than the narrow Rydberg resonances and can increase the background cross sections by orders of magnitude. The effect becomes increasingly prominent in cross sections of higher excited levels. PEC resonances exist in  $\sigma_{PI}$  of *all* excited bound levels



**Figure 3.** Level-specific recombination rate coefficient,  $\alpha_R(T, nSLJ)$ , of the ground and excited Rydberg series of levels,  $1s^2 n s (2S^{1/2})$  with  $2 \leq n \leq 6$ , of S XIV. The shoulder at high temperature is due to DR or resonances in  $\sigma_{PI}$  in the high energy region.

of S XIV.

The partial cross sections also show PEC resonances due to core excitation. However, the partial cross sections have lower background cross sections and less resonances as exemplified in Figure 1.

*4.1.2. Electron-ion Recombination* Level-specific recombination rate coefficients,  $\alpha_R(T, nSLJ)$ , that include both the RR and DR, are presented for all 98 fine structure levels of S XIV. Typical feature of these rates show smooth decay with a DR ‘shoulder’

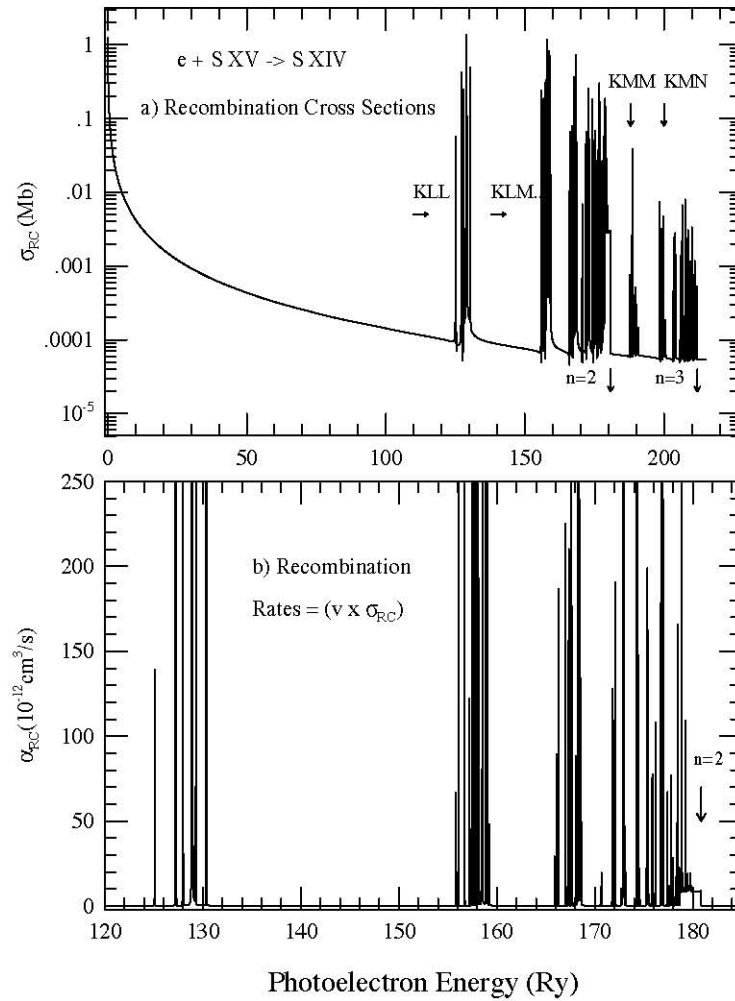


**Figure 4.** (a) Total unified (e + ion) recombination cross sections,  $\sigma_{RC}$ , and (b) unified recombination rate coefficients,  $\alpha_{RC}(E)$ , with photoelectron energy for (e + S XV  $\rightarrow$  S XIV). Separated resonance complexes, KLL, KLM, etc of  $n = 2$  and KMM, etc. of  $n = 3$  thresholds are noted.  $\alpha_{RC}(E)$  with high resonances below  $n=2$  thresholds can be measured at labs.

at high temperature. The shoulder is formed from DR or the resonances in the high energy region. Figure 3 shows level-specific recombination rate coefficients for ground and excited levels of the series,  $1s^2ns(^2S_{1/2})$  where  $2 \leq n \leq 6$ .

Table 2 presents numerical values of  $\alpha_R(T, nSLJ)$  for recombining to the ground and lowest seven excited  $n = 2$  and 3 levels of S XIV:  $1s^22s \ ^2S_0$ ,  $1s^23s \ ^2S_0$ ,  $1s^22p \ ^2P_{1/2}^o$ ,  $1s^23p \ ^2P_{1/2}^o$ ,  $1s^23d \ ^2D_{3/2}$ ,  $1s^22p \ ^2P_{3/2}^o$ ,  $1s^23p \ ^2P_{3/2}^o$ ,  $1s^23d \ ^2D_{3/2}$ ,  $1s^23d \ ^2D_{5/2}$ . Spectral modeling in the UV region requires these rates.

The total unified recombination cross sections  $\sigma_{RC}(E)$  and the recombination rate

**Table 2.** Level specific recombination rate coefficients for the ground and excited  $2l$  and  $3l$  levels of S XIV. BE is the binding energy of the level in Rydberg.

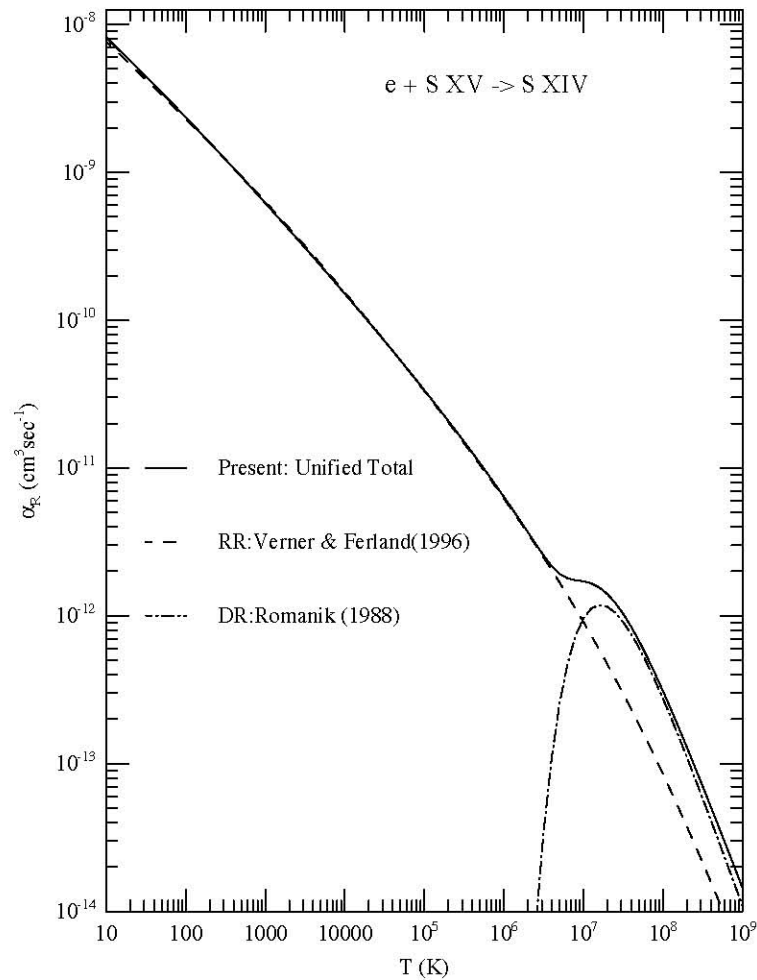
$\log_{10}T$ (K)	$\alpha_R (cm^3 s^{-1})$							
	$2s \ ^2S_{1/2}$	$3s \ ^2S_{1/2}$	$2p \ ^2P_{1/2}^o$	$3p \ ^2P_{1/2}^o$	$3d \ ^2D_{3/2}$	$2p \ ^2P_{3/2}^o$	$3p \ ^2P_{3/2}^o$	$3d \ ^2D_{5/2}$
BE=	-52.0	-22.6	-49.9	-22.1	-21.8	-49.8	-22.0	-21.8
1.0	1.47E-10	4.80E-11	1.48E-10	5.46E-11	7.29E-11	2.93E-10	1.09E-10	1.09E-10
1.1	1.31E-10	4.27E-11	1.32E-10	4.87E-11	6.50E-11	2.61E-10	9.69E-11	9.72E-11
1.2	1.17E-10	3.81E-11	1.18E-10	4.34E-11	5.79E-11	2.33E-10	8.64E-11	8.66E-11
1.3	1.04E-10	3.40E-11	1.05E-10	3.87E-11	5.16E-11	2.08E-10	7.70E-11	7.72E-11
1.4	9.30E-11	3.03E-11	9.34E-11	3.45E-11	4.60E-11	1.85E-10	6.86E-11	6.88E-11
1.5	8.29E-11	2.70E-11	8.33E-11	3.07E-11	4.10E-11	1.65E-10	6.12E-11	6.13E-11
1.6	7.39E-11	2.40E-11	7.42E-11	2.74E-11	3.66E-11	1.47E-10	5.45E-11	5.46E-11
1.7	6.58E-11	2.14E-11	6.62E-11	2.44E-11	3.26E-11	1.31E-10	4.86E-11	4.87E-11
1.8	5.87E-11	1.91E-11	5.90E-11	2.17E-11	2.90E-11	1.17E-10	4.33E-11	4.34E-11
1.9	5.23E-11	1.70E-11	5.25E-11	1.94E-11	2.59E-11	1.04E-10	3.86E-11	3.87E-11
2.0	4.66E-11	1.52E-11	4.68E-11	1.73E-11	2.31E-11	9.27E-11	3.44E-11	3.45E-11
2.1	4.15E-11	1.35E-11	4.17E-11	1.54E-11	2.06E-11	8.26E-11	3.07E-11	3.07E-11
2.2	3.70E-11	1.20E-11	3.72E-11	1.37E-11	1.83E-11	7.37E-11	2.73E-11	2.74E-11
2.3	3.30E-11	1.07E-11	3.32E-11	1.22E-11	1.63E-11	6.56E-11	2.44E-11	2.44E-11
2.4	2.94E-11	9.57E-12	2.95E-11	1.09E-11	1.46E-11	5.85E-11	2.17E-11	2.17E-11
2.5	2.62E-11	8.53E-12	2.63E-11	9.71E-12	1.30E-11	5.21E-11	1.93E-11	1.94E-11
2.6	2.34E-11	7.60E-12	2.35E-11	8.66E-12	1.16E-11	4.65E-11	1.72E-11	1.73E-11
2.7	2.08E-11	6.78E-12	2.09E-11	7.72E-12	1.03E-11	4.14E-11	1.54E-11	1.54E-11
2.8	1.86E-11	6.04E-12	1.86E-11	6.88E-12	9.18E-12	3.69E-11	1.37E-11	1.37E-11
2.9	1.65E-11	5.38E-12	1.66E-11	6.13E-12	8.18E-12	3.29E-11	1.22E-11	1.22E-11
3.0	1.47E-11	4.80E-12	1.48E-11	5.46E-12	7.29E-12	2.93E-11	1.09E-11	1.09E-11
3.1	1.31E-11	4.28E-12	1.32E-11	4.87E-12	6.50E-12	2.61E-11	9.69E-12	9.71E-12
3.2	1.17E-11	3.81E-12	1.18E-11	4.34E-12	5.79E-12	2.33E-11	8.64E-12	8.65E-12
3.3	1.04E-11	3.40E-12	1.05E-11	3.87E-12	5.16E-12	2.08E-11	7.70E-12	7.71E-12
3.4	9.30E-12	3.03E-12	9.34E-12	3.45E-12	4.60E-12	1.85E-11	6.86E-12	6.87E-12
3.5	8.29E-12	2.70E-12	8.33E-12	3.07E-12	4.10E-12	1.65E-11	6.11E-12	6.12E-12
3.6	7.39E-12	2.40E-12	7.42E-12	2.74E-12	3.65E-12	1.47E-11	5.45E-12	5.45E-12
3.7	6.58E-12	2.14E-12	6.61E-12	2.44E-12	3.25E-12	1.31E-11	4.86E-12	4.86E-12
3.8	5.87E-12	1.91E-12	5.89E-12	2.17E-12	2.90E-12	1.17E-11	4.33E-12	4.33E-12
3.9	5.23E-12	1.70E-12	5.25E-12	1.94E-12	2.58E-12	1.04E-11	3.86E-12	3.86E-12
4.0	4.66E-12	1.52E-12	4.68E-12	1.73E-12	2.30E-12	9.26E-12	3.44E-12	3.43E-12
4.1	4.15E-12	1.35E-12	4.17E-12	1.54E-12	2.05E-12	8.25E-12	3.06E-12	3.06E-12
4.2	3.70E-12	1.21E-12	3.71E-12	1.37E-12	1.82E-12	7.35E-12	2.73E-12	2.72E-12
4.3	3.30E-12	1.07E-12	3.31E-12	1.22E-12	1.62E-12	6.55E-12	2.43E-12	2.42E-12
4.4	2.94E-12	9.58E-13	2.95E-12	1.09E-12	1.44E-12	5.83E-12	2.16E-12	2.15E-12
4.5	2.62E-12	8.54E-13	2.62E-12	9.68E-13	1.28E-12	5.19E-12	1.93E-12	1.91E-12
4.6	2.34E-12	7.61E-13	2.34E-12	8.62E-13	1.14E-12	4.62E-12	1.72E-12	1.70E-12
4.7	2.08E-12	6.78E-13	2.08E-12	7.67E-13	1.01E-12	4.12E-12	1.53E-12	1.51E-12
4.8	1.86E-12	6.05E-13	1.85E-12	6.83E-13	8.95E-13	3.66E-12	1.36E-12	1.34E-12
4.9	1.66E-12	5.39E-13	1.65E-12	6.08E-13	7.93E-13	3.26E-12	1.21E-12	1.18E-12
5.0	1.48E-12	4.81E-13	1.46E-12	5.40E-13	7.01E-13	2.90E-12	1.08E-12	1.05E-12
5.1	1.32E-12	4.29E-13	1.30E-12	4.80E-13	6.18E-13	2.57E-12	9.56E-13	9.24E-13
5.2	1.17E-12	3.82E-13	1.15E-12	4.26E-13	5.45E-13	2.28E-12	8.49E-13	8.14E-13
5.3	1.05E-12	3.41E-13	1.02E-12	3.78E-13	4.78E-13	2.03E-12	7.53E-13	7.14E-13
5.4	9.34E-13	3.04E-13	9.07E-13	3.35E-13	4.18E-13	1.80E-12	6.67E-13	6.25E-13
5.5	8.34E-13	2.72E-13	8.02E-13	2.97E-13	3.65E-13	1.59E-12	5.91E-13	5.45E-13
5.6	7.44E-13	2.42E-13	7.09E-13	2.62E-13	3.16E-13	1.40E-12	5.22E-13	4.73E-13
5.7	6.64E-13	2.16E-13	6.24E-13	2.31E-13	2.73E-13	1.23E-12	4.60E-13	4.08E-13
5.8	5.93E-13	1.93E-13	5.49E-13	2.03E-13	2.34E-13	1.09E-12	4.04E-13	3.50E-13
5.9	5.29E-13	1.72E-13	4.81E-13	1.78E-13	1.99E-13	9.51E-13	3.54E-13	2.98E-13
6.0	4.73E-13	1.54E-13	4.19E-13	1.56E-13	1.68E-13	8.30E-13	3.09E-13	2.52E-13
6.1	4.22E-13	1.37E-13	3.65E-13	1.35E-13	1.41E-13	7.21E-13	2.69E-13	2.11E-13
6.2	3.76E-13	1.22E-13	3.15E-13	1.17E-13	1.17E-13	6.23E-13	2.32E-13	1.75E-13
6.3	3.36E-13	1.09E-13	2.71E-13	1.01E-13	9.65E-14	5.37E-13	2.00E-13	1.44E-13
6.4	3.00E-13	9.66E-14	2.34E-13	8.61E-14	7.87E-14	4.62E-13	1.71E-13	1.17E-13
6.5	2.70E-13	8.63E-14	2.04E-13	7.37E-14	6.40E-14	4.05E-13	1.46E-13	9.47E-14
6.6	2.48E-13	7.86E-14	1.85E-13	6.40E-14	5.28E-14	3.72E-13	1.26E-13	7.61E-14
6.7	2.33E-13	7.44E-14	1.78E-13	5.81E-14	4.59E-14	3.68E-13	1.12E-13	6.13E-14
6.8	2.24E-13	7.39E-14	1.81E-13	5.59E-14	4.33E-14	3.87E-13	1.05E-13	5.01E-14
6.9	2.17E-13	7.58E-14	1.88E-13	5.64E-14	4.36E-14	4.13E-13	1.03E-13	4.19E-14
7.0	2.08E-13	7.77E-14	1.92E-13	5.76E-14	4.51E-14	4.32E-13	1.02E-13	3.56E-14

Table 2 continues.

$\log_{10} T$ (K)	$\alpha_R (cm^3 s^{-1})$							
	$2s^2S_{1/2}$	$3s^2S_{1/2}$	$2p^2P_{1/2}^o$	$3p^2P_{1/2}^o$	$3d^2D_{3/2}$	$2p^2P_{3/2}^o$	$3p^2P_{3/2}^o$	$3d^2D_{5/2}$
7.1	1.95E-13	7.77E-14	1.89E-13	5.75E-14	4.58E-14	4.32E-13	1.00E-13	3.06E-14
7.2	1.78E-13	7.47E-14	1.77E-13	5.53E-14	4.46E-14	4.10E-13	9.47E-14	2.62E-14
7.3	1.58E-13	6.88E-14	1.59E-13	5.08E-14	4.14E-14	3.71E-13	8.61E-14	2.21E-14
7.4	1.36E-13	6.08E-14	1.36E-13	4.47E-14	3.67E-14	3.21E-13	7.53E-14	1.82E-14
7.5	1.14E-13	5.19E-14	1.13E-13	3.79E-14	3.12E-14	2.68E-13	6.35E-14	1.47E-14
7.6	9.34E-14	4.30E-14	9.16E-14	3.11E-14	2.56E-14	2.17E-13	5.19E-14	1.17E-14
7.7	7.53E-14	3.48E-14	7.22E-14	2.48E-14	2.04E-14	1.72E-13	4.14E-14	9.09E-15
7.8	5.98E-14	2.75E-14	5.59E-14	1.94E-14	1.59E-14	1.33E-13	3.23E-14	6.95E-15
7.9	4.69E-14	2.14E-14	4.26E-14	1.49E-14	1.22E-14	1.01E-13	2.48E-14	5.25E-15
8.0	3.64E-14	1.65E-14	3.20E-14	1.13E-14	9.19E-15	7.61E-14	1.88E-14	3.92E-15
8.1	2.80E-14	1.25E-14	2.39E-14	8.43E-15	6.83E-15	5.66E-14	1.41E-14	2.90E-15
8.2	2.14E-14	9.46E-15	1.76E-14	6.25E-15	5.04E-15	4.18E-14	1.04E-14	2.13E-15
8.3	1.63E-14	7.09E-15	1.30E-14	4.60E-15	3.68E-15	3.07E-14	7.69E-15	1.55E-15
8.4	1.23E-14	5.28E-15	9.47E-15	3.37E-15	2.68E-15	2.24E-14	5.63E-15	1.13E-15
8.5	9.29E-15	3.92E-15	6.89E-15	2.45E-15	1.93E-15	1.63E-14	4.11E-15	8.15E-16
8.6	6.97E-15	2.90E-15	5.00E-15	1.78E-15	1.39E-15	1.18E-14	2.99E-15	5.88E-16
8.7	5.21E-15	2.13E-15	3.62E-15	1.29E-15	1.00E-15	8.52E-15	2.17E-15	4.23E-16
8.8	3.89E-15	1.57E-15	2.62E-15	9.32E-16	7.16E-16	6.14E-15	1.57E-15	3.04E-16
8.9	2.89E-15	1.15E-15	1.89E-15	6.72E-16	5.12E-16	4.42E-15	1.13E-15	2.18E-16
9.0	2.15E-15	8.43E-16	1.36E-15	4.83E-16	3.65E-16	3.18E-15	8.16E-16	1.56E-16

coefficient with photoelectron energy  $\alpha_{RC}(E)$  are presented as both are considerable interest. Detailed  $\sigma_{RC}(E)$  provides the spectrum of dielectronic satellite lines used for diagnostics of astrophysical thin plasmas while  $\alpha_{RC}(E)$  is of experimental interest since it can be measured in synchrotron based set-ups, such as Test Storage Ring (TSR) in Heidelberg (e.g. Schippers et al. 2001). Both  $\sigma_{RC}(E)$  and  $\alpha_{RC}(E)$  for the recombined S XIV are presented in the top and the bottom panels of Figure 4.  $\sigma_{RC}$  diverges at zero photoelectron energy, but decays fast smoothly with energy until the emergence of resonance complexes at high energies. A few resonance complexes are marked in the figures, such as KLL, KLM converging on to  $n = 2$  thresholds, and KMM, KMN etc., converging on to  $n = 3$  thresholds. These resonances, especially the KLL resonances manifest themselves as di-electronic satellite lines observed in tokomaks, TSR, Electron-Beam-Ion-Traps (EBIT), and high temperature astrophysical sources. The profiles and intensities from the unified cross sections can be directly compared with measured quantities and observed recombination spectra of satellite lines (Nahar & Pradhan 2006). Figure 4(b) presents  $\alpha_{RC}(E)$  in the energy range where the resonances converge on to the  $n = 2$  threshold. Experiments can be carried in this energy range and hence the Y-scaling is chosen to be linear. In experimental measurements the strong narrow resonances are convolved with the monochromatic bandwidth of the detector and hence appear broader.

The total recombination rate coefficient  $\alpha_{RC}(T)$  for S XIV is given for a wide range of temperature in Table 3. The main features are illustrated and compared with the available data for RR and DR rates in Figures 5. The unified  $\alpha_{RC}(T)$  (solid) shows the basic features. Starting high in the very low temperature, the rate goes down until it rises to form a DR "bump" at high temperature which is followed by a monotonic decay. The low temperature recombination is dominated by radiative recombination into an infinite



**Figure 5.** Total unified recombination rate coefficients  $\alpha_R(T)$  (solid curve) for ( $e + S XV \rightarrow S XIV$ ). The RR rates are by Verner and Ferland (1996) (dash) and the DR rates are by Romanik (1988, dot-dash).

number of of high- $n$  levels resulting in a smooth decay. The temperature "bump" is due to appearance of resonances and the consequent dominance of DR. Present rate shows very good agreement with previous results as expected for highly charged few electron systems. Due to RR domination at low temperature, present total rate agrees with the RR rates from central-field approximation by Verner and Ferland (1996, dashed curve). The agreement at high temperature is also very good with the DR rate from isolated resonance approximation by Romanik (1988, dot-dash), even at the temperature region of RR and DR interference where the sum of earlier RR and DR rates equals to the total unified rate. The interference between RR and DR is negligible for S XIV.

Table 3. Total recombination rate coefficients  $\alpha_R(T)$  for S XIV, S XV, and S XVI.

$\log_{10}T$ K	$\alpha_R(cm^3 s^{-1})$		
	S XIV	S XV	S XVI
1.0	8.18E-09	9.96E-09	1.20E-08
1.1	7.25E-09	8.84E-09	1.07E-08
1.2	6.42E-09	7.83E-09	9.47E-09
1.3	5.69E-09	6.94E-09	8.39E-09
1.4	5.03E-09	6.15E-09	7.44E-09
1.5	4.44E-09	5.43E-09	6.58E-09
1.6	3.92E-09	4.80E-09	5.82E-09
1.7	3.46E-09	4.24E-09	5.14E-09
1.8	3.04E-09	3.74E-09	4.54E-09
1.9	2.68E-09	3.29E-09	4.00E-09
2.0	2.36E-09	2.90E-09	3.53E-09
2.1	2.07E-09	2.55E-09	3.11E-09
2.2	1.82E-09	2.24E-09	2.74E-09
2.3	1.59E-09	1.97E-09	2.41E-09
2.4	1.40E-09	1.73E-09	2.12E-09
2.5	1.22E-09	1.51E-09	1.86E-09
2.6	1.07E-09	1.33E-09	1.63E-09
2.7	9.32E-10	1.16E-09	1.43E-09
2.8	8.15E-10	1.01E-09	1.25E-09
2.9	7.10E-10	8.88E-10	1.10E-09
3.0	6.19E-10	7.75E-10	9.58E-10
3.1	5.40E-10	6.77E-10	8.38E-10
3.2	4.70E-10	5.90E-10	7.33E-10
3.3	4.09E-10	5.15E-10	6.40E-10
3.4	3.55E-10	4.48E-10	5.59E-10
3.5	3.08E-10	3.90E-10	4.88E-10
3.6	2.68E-10	3.40E-10	4.24E-10
3.7	2.32E-10	2.96E-10	3.71E-10
3.8	2.01E-10	2.57E-10	3.23E-10
3.9	1.74E-10	2.23E-10	2.81E-10
4.0	1.51E-10	1.94E-10	2.45E-10
4.1	1.30E-10	1.68E-10	2.13E-10
4.2	1.13E-10	1.46E-10	1.85E-10
4.3	9.73E-11	1.26E-10	1.61E-10
4.4	8.39E-11	1.09E-10	1.39E-10
4.5	7.22E-11	9.44E-11	1.21E-10
4.6	6.22E-11	8.15E-11	1.05E-10
4.7	5.34E-11	7.04E-11	9.09E-11
4.8	4.58E-11	6.07E-11	7.86E-11
4.9	3.92E-11	5.23E-11	6.80E-11
5.0	3.36E-11	4.50E-11	5.87E-11
5.1	2.87E-11	3.87E-11	5.07E-11
5.2	2.45E-11	3.33E-11	4.38E-11
5.3	2.09E-11	2.85E-11	3.77E-11
5.4	1.77E-11	2.44E-11	3.25E-11
5.5	1.50E-11	2.09E-11	2.79E-11
5.6	1.27E-11	1.79E-11	2.39E-11
5.7	1.07E-11	1.53E-11	2.06E-11
5.8	9.06E-12	1.30E-11	1.76E-11
5.9	7.61E-12	1.11E-11	1.51E-11
6.0	6.38E-12	9.39E-12	1.29E-11
6.1	5.34E-12	7.96E-12	1.10E-11
6.2	4.45E-12	6.73E-12	9.36E-12
6.3	3.70E-12	5.68E-12	7.96E-12
6.4	3.07E-12	4.79E-12	6.75E-12
6.5	2.56E-12	4.04E-12	5.72E-12
6.6	2.17E-12	3.43E-12	4.82E-12
6.7	1.92E-12	2.96E-12	4.08E-12
6.8	1.79E-12	2.62E-12	3.43E-12
6.9	1.74E-12	2.38E-12	2.87E-12
7.0	1.71E-12	2.20E-12	2.40E-12



Table 3 continues.

$\log_{10}T$ K	$\alpha_R(cm^3 s^{-1})$		
	S XIV	S XV	S XVI
7.1	1.66E-12	2.02E-12	2.00E-12
7.2	1.56E-12	1.84E-12	1.66E-12
7.3	1.41E-12	1.64E-12	1.37E-12
7.4	1.23E-12	1.42E-12	1.13E-12
7.5	1.03E-12	1.20E-12	9.26E-13
7.6	8.45E-13	9.87E-13	7.53E-13
7.7	6.75E-13	7.98E-13	6.12E-13
7.8	5.29E-13	6.34E-13	4.93E-13
7.9	4.08E-13	4.97E-13	3.95E-13
8.0	3.10E-13	3.85E-13	3.15E-13
8.1	2.34E-13	2.96E-13	2.49E-13
8.2	1.74E-13	2.25E-13	1.96E-13
8.3	1.29E-13	1.71E-13	1.53E-13
8.4	9.56E-14	1.29E-13	1.19E-13
8.5	7.02E-14	9.65E-14	9.23E-14
8.6	5.14E-14	7.22E-14	7.06E-14
8.7	3.76E-14	5.38E-14	5.43E-14
8.8	2.74E-14	4.00E-14	4.11E-14
8.9	1.99E-14	2.97E-14	3.11E-14
9.0	1.45E-14	2.20E-14	2.34E-14

#### 4.2. S XV

For He-like S XV, a total of 188 bound fine structure levels of total angular momenta  $0 \leq J \leq 10$  with  $n \leq 10$ ,  $0 \leq l \leq 9$ ,  $0 \leq L \leq 14$  are found. The energies agree very well, in less than 1%, with the available observed energies compiled by NIST.

*4.2.1. Photoionization* Total photoionization cross sections for S XV, leaving the target or core ion in the ground and 15 excited levels, are presented for all 188 bound levels. Partial photoionization cross sections leaving the target in the ground level are also obtained for all these fine structure levels.

Illustrative features of the total  $\sigma_{PI}$  of the ground and low lying excited levels, especially those corresponding to the four most commonly used spectral diagnostic lines (w,x,y,z) of He-like ions, are shown in Figure 6. The top panel (a) presents  $\sigma_{PI}$  of the ground level  $1s^2 ({}^1S_0)$ . The lower four panels present level-specific cross sections of the four lowest  $n = 2$  excited levels that give rise to prominent X-ray lines in the  $K\alpha$  complex: (b) the resonance line (w:  $1s^2 ({}^1S_0) \leftarrow 1s2p({}^1P_1^o)$ ), (c) forbidden line (x:  $1s^2 ({}^1S_0) \leftarrow 1s2p({}^3P_2^o)$ ), (d) intercombination line (y :  $1s^2 ({}^1S_0) \leftarrow 1s2p({}^3P_1^o)$ ), and (e) forbidden line (z:  $1s^2 ({}^1S_0) \leftarrow 1s2s({}^3S_1)$ ). These lines are also known as the *r*, *f*, *i*, *f* lines. Their ratios provide information of temperature, density, ionization balance, and abundances in plasma sources.

The curves in Figure 6 show that the cross section  $\sigma_{PI}$  decreases monotonically over a large energy range for all levels. The resonances in photoionization cross sections appear in high energy due to Rydberg series of autoionizing states belong to high lying core levels.  $\sigma_{PI}$  of the ground level  $1s^2({}^1S_0)$  has smooth background with some narrow resonances belonging to  $n=2$  thresholds. However, much more resonances show up in excited state  $\sigma_{PI}$ . The well-separated resonance complexes are LL (2l2l), LM (2l3l') etc

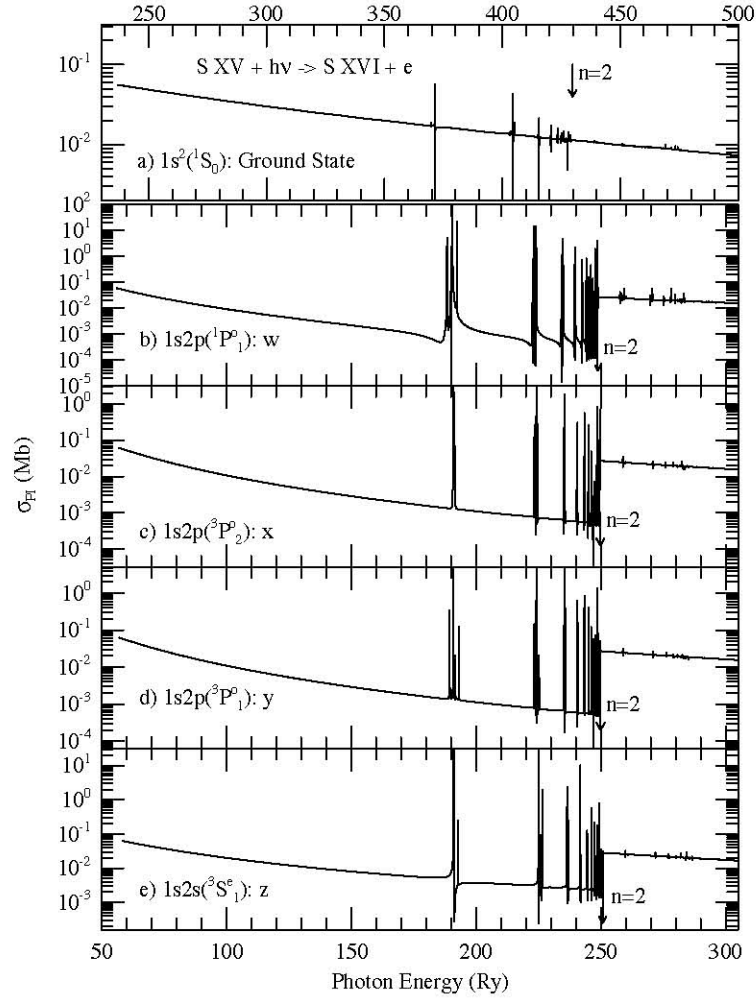
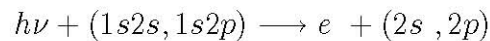


**Figure 6.** Level-specific photoionization cross sections of S XV: (a) the ground level,  $1s^2(1S_0)$ , and four excited (b)  $1s2p(1P_1^o)$ , (c)  $1s2p(3P_2^o)$ , (d)  $1s2p(3P_1^o)$ , (e)  $1s2s(3S_1^e)$  levels corresponding to the prominent resonance (w), intercombination (y), and forbidden(x,z) diagnostic X-ray lines. K-shell ionization edge for excited levels is marked at  $n = 2$  thresholds.

converging on to  $n=2$  thresholds of the core. In contrast to the ground level, the excited levels show a K-shell jump at the  $n = 2$  threshold due to  $1s$  ionization:



Ground level does not have an excited core electron to introduce such a bump.

Comparison of the present  $\sigma_{PI}$  with those from the OP (Fernly et al. 1987) is made in Figure 7. OP does not consider fine structure levels. Hence the ground level  $1s^2(1S_0)$  and excited level  $1s2p(1P_1^o)$  are chosen as they represent the same state in fine structure

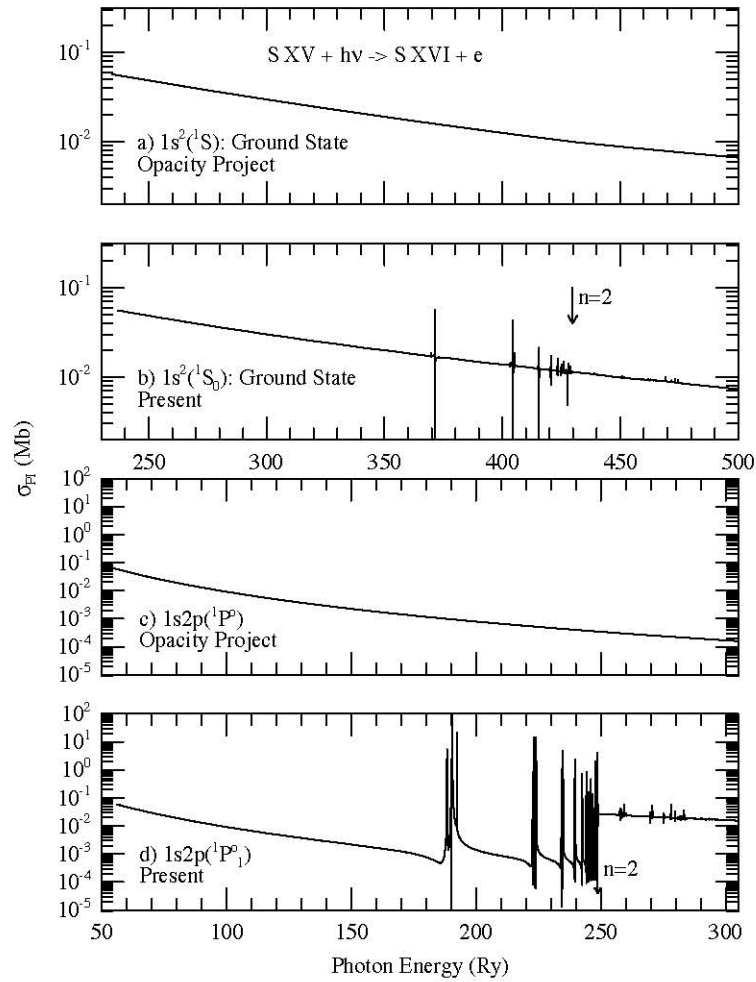


**Figure 7.** Comparison of photoionization cross sections of S XV of the ground level,  $1s^2(1S_0)$  (panel a - Opacity Project and panel b - present) and excited level,  $1s2p(1P_1^o)$ , (panel c - Opacity Project, d - present). The features seen in present  $\sigma_{PI}$  are missing in the OP data.

and in LS coupling term. Although both OP and present  $\sigma_{PI}$  are very much similar for the ground level, the resonances and their positions are missing in the OP data. It is important to know the positions of the resonances and their relative strengths since these may be observed as absorption lines in the X-ray spectra. The large difference between the present and OP results is seen for the excited state where OP cross sections miss out all the resonant features as well as the enhancement in the background.

Similar to the excited levels of the Li-like S XIV,  $\sigma_{PI}$  of excited levels of He-like S XV exhibit PEC resonances. Figure 8 presents level specific total  $\sigma_{PI}$  of the

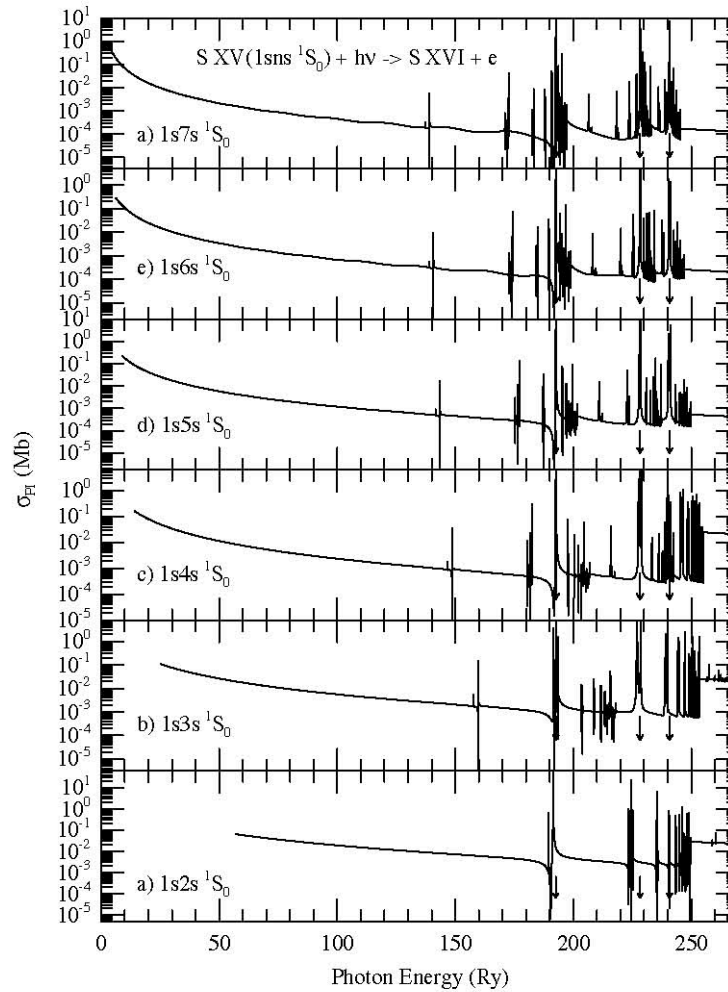


**Figure 8.** Total photoionization cross sections of the excited Rydberg series of levels,  $1sns(^1S_0)$  with  $2 \leq n \leq 7$ , of S XIV. The figure illustrates the prominent PEC (*photoexcitation-of-core*) resonances (pointed by arrows) at about 192 Ry due to excitations of  $n=2$  core levels  $2p \ ^2P_{1/2,3/2}^o$ , at about 228 Ry due to  $n=3$  core levels  $3p \ ^2P_{1/2,3/2}^o$ , and at about 241 Ry due to  $n=4$  core levels  $4p \ ^2P_{1/2,3/2}^o$ .

excited Rydberg series of levels,  $1sns(^1S_0)$  with  $2 \leq n \leq 7$  for S XV. The enhanced PEC resonance positions are pointed by arrows at photon energies 192 Ry due to core excitations to  $n=2$  levels,  $2s \ ^2S_{1/2} - 2p \ ^2P_{1/2,3/2}^o$ , at about 228 Ry for transitions to  $n=3$  levels  $2s \ ^2S_{1/2} - 3p \ ^2P_{1/2,3/2}^o$ , and at about 241 Ry for transitions to  $n=4$  levels  $2s \ ^2S_{1/2} - 4p \ ^2P_{1/2,3/2}^o$ . The enhanced background due to PEC are clear from that of narrow Rydberg autoionizing resonances. PEC resonances become distinct with higher  $n$ .

Partial photoionization cross sections for S XV do not include contributions from channels of excited core ionization. Hence, although similar to those of the total, they have less resonances and lower background.

*4.2.2. Electron-ion recombination* Level-specific recombination rate coefficients  $\alpha_R(nSLJ)$  are presented for all 188 fine structure levels of S XV with  $0 \leq J \leq 10$  and  $n \leq 10$ . Table 4 presents a sample set of level specific recombination rates for the ground level  $1s^2(1S_0)$ , and excited levels  $1s2s(1S_0)$ ,  $1s2s(3S_1)$ ,  $1s2p(1P_1^o)$ ,  $1s2p(3P_0^o)$ ,  $1s2p(3P_1^o)$ ,  $1s2p(3P_2^o)$ ,  $1s3s(1S_0)$ , and  $1s3s(3S_1)$ . The set includes the levels corresponding to the X-ray w, x, y, and z lines of S XV. The rates show a smooth decay, similar to S XIV, and a small shoulder at high temperature due to DR resonances.

The total unified electron-ion recombination collision strength ( $\Omega_{RC}$ ), total recombination cross sections ( $\sigma_{RC}$ ) and recombination rate coefficients ( $\alpha_{RC}(E)$ ) are presented. Since  $\Omega_{RC}$  and  $\sigma_{RC}$  differ by some kinematic factors, they show similar features. Figure 9 presents  $\sigma_{RC}$  in the top panel and  $\alpha_{RC}(E)$  in the bottom panel. Similar to Li-like S XIV, the unified  $\sigma_{RC}$  of He-like S XV, in Figure 9(a), decays smoothly with energy until resonance complexes appear at very high energies. It also shows separated resonance complexes, such as LL (2l2l'), LM (2l3l'), etc. converging on to the  $n = 2$  thresholds, MM, MN etc. converging on to the  $n = 3$  thresholds, etc. LL, LM complexes are seen as dielectronic satellite lines in recombination spectra. The resonances become much weaker by orders of magnitude and narrower beyond  $n = 2$  thresholds, and hence become less important. The resonances for the velocity dependent photorecombination rate  $\alpha_{RC}(E)$  for S XV are strong up to  $n=2$  threshold, shown in Figure 9(b), and hence are expected to be seen in experiment.

Total unified recombination rate coefficients  $\alpha_R(T)$  for S XV are presented for a wide range of temperature,  $1 \leq \log_{10}T \leq 9$ , in Table 3. The features are illustrated and compared with the available rates in Figure 10. The unified  $\alpha_R(T)$  (solid) shows features similar to S XIV. The low temperature rate is high due to dominance of RR in to an infinite number of high-n levels and decreases over a wide temperature range since the autoionizing resonances do not appear until at high energy.  $\alpha_R(T)$  forms a small "bump" at high temperature due to dominant DR process, and decays smoothly. The present total  $\alpha_R(T)$  S XV agrees very well with the RR rate coefficients by Verner and Ferland (1996, dash) and high temperature DR rates from isolated resonance approximation by Romanik (1988, dot). However, the fit by Shull and Steenberg (1982, short dash) for S XV peaks lower.

Recombination rates for H-like S XVI are provided in Table 3 for completeness. Photoionization cross sections of S XVI are also available electronically.

## 5. Conclusion

The inverse processes of photoionization and electron-ion recombination for S XIV and S XV are studied in detail using the unified method for total recombination. The ions

Table 4. Level specific recombination rate coefficients  $\alpha_R(nJ\pi)$  for the ground and excited  $2l$  and  $3s$  levels of S XV. BE is the binding energy of the level in Rydberg.

$\log_{10}T$ (K)	$\alpha_R(\text{cm}^3\text{s}^{-1})$								
	$1s^2\ ^1S_0$	$1s2s\ ^1S_0$	$1s3s\ ^1S_0$	$1s2p\ ^3P_0^o$	$1s2s\ ^3S_1$	$1s3s\ ^3S_1$	$1s2p\ ^3P_1^o$	$1s2p\ ^1P_1^o$	$1s2p\ ^3P_2^o$
BE=	-237.	-57.0	-25.3	-57.2	-58.3	-25.6	-57.1	-56.1	-57.0
1.0	6.46E-10	4.29E-11	1.43E-11	4.20E-11	1.33E-10	4.32E-11	1.26E-10	1.15E-10	2.08E-10
1.1	5.76E-10	3.82E-11	1.27E-11	3.75E-11	1.18E-10	3.85E-11	1.13E-10	1.02E-10	1.85E-10
1.2	5.14E-10	3.41E-11	1.13E-11	3.34E-11	1.05E-10	3.43E-11	1.00E-10	9.11E-11	1.65E-10
1.3	4.58E-10	3.04E-11	1.01E-11	2.98E-11	9.38E-11	3.06E-11	8.94E-11	8.12E-11	1.47E-10
1.4	4.08E-10	2.71E-11	9.00E-12	2.65E-11	8.36E-11	2.73E-11	7.97E-11	7.23E-11	1.31E-10
1.5	3.64E-10	2.41E-11	8.02E-12	2.36E-11	7.45E-11	2.43E-11	7.10E-11	6.45E-11	1.17E-10
1.6	3.24E-10	2.15E-11	7.15E-12	2.11E-11	6.64E-11	2.17E-11	6.33E-11	5.75E-11	1.04E-10
1.7	2.89E-10	1.92E-11	6.37E-12	1.88E-11	5.92E-11	1.93E-11	5.64E-11	5.12E-11	9.29E-11
1.8	2.57E-10	1.71E-11	5.68E-12	1.67E-11	5.28E-11	1.72E-11	5.03E-11	4.56E-11	8.28E-11
1.9	2.29E-10	1.52E-11	5.06E-12	1.49E-11	4.70E-11	1.53E-11	4.48E-11	4.07E-11	7.38E-11
2.0	2.04E-10	1.36E-11	4.51E-12	1.33E-11	4.19E-11	1.37E-11	3.99E-11	3.63E-11	6.57E-11
2.1	1.82E-10	1.21E-11	4.02E-12	1.18E-11	3.74E-11	1.22E-11	3.56E-11	3.23E-11	5.86E-11
2.2	1.62E-10	1.08E-11	3.58E-12	1.06E-11	3.33E-11	1.09E-11	3.17E-11	2.88E-11	5.22E-11
2.3	1.45E-10	9.60E-12	3.19E-12	9.41E-12	2.97E-11	9.67E-12	2.83E-11	2.57E-11	4.65E-11
2.4	1.29E-10	8.56E-12	2.85E-12	8.39E-12	2.64E-11	8.62E-12	2.52E-11	2.29E-11	4.15E-11
2.5	1.15E-10	7.63E-12	2.54E-12	7.47E-12	2.36E-11	7.68E-12	2.25E-11	2.04E-11	3.70E-11
2.6	1.02E-10	6.80E-12	2.26E-12	6.66E-12	2.10E-11	6.85E-12	2.00E-11	1.82E-11	3.29E-11
2.7	9.13E-11	6.06E-12	2.01E-12	5.94E-12	1.87E-11	6.10E-12	1.78E-11	1.62E-11	2.94E-11
2.8	8.14E-11	5.40E-12	1.80E-12	5.29E-12	1.67E-11	5.44E-12	1.59E-11	1.44E-11	2.62E-11
2.9	7.25E-11	4.81E-12	1.60E-12	4.72E-12	1.49E-11	4.85E-12	1.42E-11	1.29E-11	2.33E-11
3.0	6.46E-11	4.29E-12	1.43E-12	4.20E-12	1.33E-11	4.32E-12	1.26E-11	1.15E-11	2.08E-11
3.1	5.76E-11	3.82E-12	1.27E-12	3.75E-12	1.18E-11	3.85E-12	1.13E-11	1.02E-11	1.85E-11
3.2	5.14E-11	3.41E-12	1.13E-12	3.34E-12	1.05E-11	3.43E-12	1.00E-11	9.11E-12	1.65E-11
3.3	4.58E-11	3.04E-12	1.01E-12	2.97E-12	9.38E-12	3.06E-12	8.94E-12	8.11E-12	1.47E-11
3.4	4.08E-11	2.71E-12	9.00E-13	2.65E-12	8.36E-12	2.73E-12	7.97E-12	7.23E-12	1.31E-11
3.5	3.64E-11	2.41E-12	8.02E-13	2.36E-12	7.45E-12	2.43E-12	7.10E-12	6.44E-12	1.17E-11
3.6	3.24E-11	2.15E-12	7.15E-13	2.11E-12	6.64E-12	2.17E-12	6.33E-12	5.74E-12	1.04E-11
3.7	2.89E-11	1.92E-12	6.37E-13	1.88E-12	5.92E-12	1.93E-12	5.64E-12	5.12E-12	9.28E-12
3.8	2.57E-11	1.71E-12	5.68E-13	1.67E-12	5.28E-12	1.72E-12	5.03E-12	4.56E-12	8.27E-12
3.9	2.29E-11	1.52E-12	5.06E-13	1.49E-12	4.70E-12	1.53E-12	4.48E-12	4.06E-12	7.37E-12
4.0	2.04E-11	1.36E-12	4.51E-13	1.33E-12	4.19E-12	1.37E-12	3.99E-12	3.62E-12	6.57E-12
4.1	1.82E-11	1.21E-12	4.02E-13	1.18E-12	3.73E-12	1.22E-12	3.56E-12	3.23E-12	5.85E-12
4.2	1.62E-11	1.08E-12	3.58E-13	1.05E-12	3.33E-12	1.09E-12	3.17E-12	2.87E-12	5.21E-12
4.3	1.45E-11	9.60E-13	3.19E-13	9.39E-13	2.97E-12	9.67E-13	2.82E-12	2.56E-12	4.64E-12
4.4	1.29E-11	8.56E-13	2.85E-13	8.36E-13	2.64E-12	8.62E-13	2.51E-12	2.28E-12	4.14E-12
4.5	1.15E-11	7.63E-13	2.54E-13	7.45E-13	2.36E-12	7.68E-13	2.24E-12	2.03E-12	3.68E-12
4.6	1.02E-11	6.80E-13	2.26E-13	6.63E-13	2.10E-12	6.85E-13	1.99E-12	1.81E-12	3.28E-12
4.7	9.13E-12	6.06E-13	2.02E-13	5.90E-13	1.87E-12	6.10E-13	1.77E-12	1.61E-12	2.92E-12
4.8	8.13E-12	5.40E-13	1.80E-13	5.25E-13	1.67E-12	5.44E-13	1.58E-12	1.43E-12	2.60E-12
4.9	7.25E-12	4.81E-13	1.60E-13	4.67E-13	1.49E-12	4.85E-13	1.40E-12	1.27E-12	2.31E-12
5.0	6.46E-12	4.29E-13	1.43E-13	4.16E-13	1.32E-12	4.32E-13	1.25E-12	1.13E-12	2.06E-12
5.1	5.75E-12	3.82E-13	1.27E-13	3.69E-13	1.18E-12	3.85E-13	1.11E-12	1.01E-12	1.83E-12
5.2	5.13E-12	3.41E-13	1.13E-13	3.28E-13	1.05E-12	3.43E-13	9.86E-13	8.94E-13	1.62E-12
5.3	4.57E-12	3.04E-13	1.01E-13	2.91E-13	9.37E-13	3.06E-13	8.75E-13	7.93E-13	1.44E-12
5.4	4.07E-12	2.71E-13	9.00E-14	2.58E-13	8.35E-13	2.73E-13	7.75E-13	7.03E-13	1.28E-12
5.5	3.62E-12	2.41E-13	8.02E-14	2.28E-13	7.44E-13	2.43E-13	6.86E-13	6.22E-13	1.13E-12
5.6	3.22E-12	2.15E-13	7.15E-14	2.02E-13	6.63E-13	2.16E-13	6.06E-13	5.49E-13	9.98E-13
5.7	2.87E-12	1.91E-13	6.36E-14	1.78E-13	5.91E-13	1.93E-13	5.35E-13	4.84E-13	8.80E-13
5.8	2.55E-12	1.70E-13	5.66E-14	1.57E-13	5.26E-13	1.72E-13	4.70E-13	4.25E-13	7.75E-13
5.9	2.27E-12	1.51E-13	5.04E-14	1.37E-13	4.68E-13	1.53E-13	4.13E-13	3.73E-13	6.80E-13
6.0	2.02E-12	1.35E-13	4.48E-14	1.20E-13	4.17E-13	1.36E-13	3.61E-13	3.25E-13	5.94E-13
6.1	1.79E-12	1.20E-13	3.98E-14	1.05E-13	3.71E-13	1.21E-13	3.14E-13	2.83E-13	5.17E-13
6.2	1.59E-12	1.06E-13	3.53E-14	9.08E-14	3.30E-13	1.07E-13	2.72E-13	2.45E-13	4.49E-13
6.3	1.41E-12	9.43E-14	3.13E-14	7.83E-14	2.93E-13	9.51E-14	2.35E-13	2.11E-13	3.87E-13
6.4	1.24E-12	8.40E-14	2.77E-14	6.72E-14	2.60E-13	8.42E-14	2.01E-13	1.82E-13	3.32E-13
6.5	1.10E-12	7.61E-14	2.46E-14	5.72E-14	2.32E-13	7.44E-14	1.72E-13	1.60E-13	2.84E-13
6.6	9.68E-13	7.19E-14	2.23E-14	4.84E-14	2.10E-13	6.57E-14	1.46E-13	1.51E-13	2.42E-13
6.7	8.51E-13	7.21E-14	2.13E-14	4.06E-14	1.94E-13	5.81E-14	1.25E-13	1.55E-13	2.08E-13
6.8	7.46E-13	7.57E-14	2.17E-14	3.39E-14	1.83E-13	5.17E-14	1.07E-13	1.70E-13	1.80E-13
6.9	6.52E-13	8.04E-14	2.32E-14	2.80E-14	1.75E-13	4.63E-14	9.22E-14	1.90E-13	1.57E-13
7.0	5.67E-13	8.34E-14	2.50E-14	2.29E-14	1.67E-13	4.14E-14	7.98E-14	2.05E-13	1.37E-13

Table 4 continues.

$\log_{10}T$ (K)	$\alpha_R(\text{cm}^3\text{s}^{-1})$								
	$1s^2\ ^1S_0$	$1s2s\ ^1S_0$	$1s3s\ ^1S_0$	$1s2p\ ^3P_0^o$	$1s2s\ ^3S_1$	$1s3s\ ^3S_1$	$1s2p\ ^3P_1^o$	$1s2p\ ^1P_1^o$	$1s2p\ ^3P_2^o$
7.1	4.90E-13	8.30E-14	2.60E-14	1.86E-14	1.57E-13	3.69E-14	6.88E-14	2.09E-13	1.19E-13
7.2	4.22E-13	7.88E-14	2.59E-14	1.50E-14	1.43E-13	3.26E-14	5.87E-14	2.01E-13	1.02E-13
7.3	3.61E-13	7.15E-14	2.45E-14	1.20E-14	1.27E-13	2.83E-14	4.93E-14	1.83E-13	8.62E-14
7.4	3.06E-13	6.24E-14	2.21E-14	9.51E-15	1.09E-13	2.42E-14	4.07E-14	1.60E-13	7.12E-14
7.5	2.58E-13	5.26E-14	1.91E-14	7.48E-15	9.20E-14	2.03E-14	3.30E-14	1.34E-13	5.77E-14
7.6	2.16E-13	4.31E-14	1.60E-14	5.85E-15	7.58E-14	1.68E-14	2.63E-14	1.09E-13	4.59E-14
7.7	1.79E-13	3.45E-14	1.30E-14	4.54E-15	6.13E-14	1.36E-14	2.07E-14	8.60E-14	3.60E-14
7.8	1.47E-13	2.72E-14	1.03E-14	3.50E-15	4.88E-14	1.10E-14	1.60E-14	6.66E-14	2.79E-14
7.9	1.20E-13	2.11E-14	8.04E-15	2.69E-15	3.84E-14	8.69E-15	1.23E-14	5.07E-14	2.14E-14
8.0	9.72E-14	1.61E-14	6.17E-15	2.06E-15	2.99E-14	6.83E-15	9.38E-15	3.81E-14	1.62E-14
8.1	7.81E-14	1.23E-14	4.69E-15	1.56E-15	2.31E-14	5.32E-15	7.09E-15	2.84E-14	1.22E-14
8.2	6.23E-14	9.24E-15	3.52E-15	1.19E-15	1.77E-14	4.12E-15	5.32E-15	2.09E-14	9.18E-15
8.3	4.94E-14	6.92E-15	2.63E-15	8.97E-16	1.35E-14	3.16E-15	3.98E-15	1.53E-14	6.85E-15
8.4	3.89E-14	5.16E-15	1.95E-15	6.75E-16	1.02E-14	2.42E-15	2.96E-15	1.12E-14	5.09E-15
8.5	3.05E-14	3.83E-15	1.44E-15	5.07E-16	7.70E-15	1.84E-15	2.20E-15	8.11E-15	3.77E-15
8.6	2.37E-14	2.84E-15	1.06E-15	3.80E-16	5.79E-15	1.39E-15	1.62E-15	5.86E-15	2.78E-15
8.7	1.84E-14	2.10E-15	7.78E-16	2.84E-16	4.33E-15	1.05E-15	1.20E-15	4.23E-15	2.05E-15
8.8	1.41E-14	1.54E-15	5.69E-16	2.12E-16	3.24E-15	7.88E-16	8.82E-16	3.05E-15	1.51E-15
8.9	1.08E-14	1.13E-15	4.15E-16	1.57E-16	2.41E-15	5.90E-16	6.48E-16	2.19E-15	1.11E-15
9.0	8.28E-15	8.32E-16	3.03E-16	1.17E-16	1.79E-15	4.41E-16	4.76E-16	1.57E-15	8.10E-16

exhibit high resonances, mainly from  $n=2$  core excitations, in the high energy region. PEC resonances enhance the background photoionization cross sections considerably for both S XIV and S XV. All these features are missing in the existing results from the Opacity Project. The total recombination rates are compared with the available RR and DR rates with good agreement.

Extensive sets of results are presented for the first time for these ions. The new results are (i) level-specific photoionization cross sections, both partial and total, with inclusion of autoionizing resonances, for levels up to  $n=10$ , (ii) level-specific recombination rate coefficients, including RR and DR, for all fine structure levels up to  $n \leq 10$  and  $0 \leq l \leq 9$ , (iii) total unified recombination rate coefficients, incorporating both RR and DR, over a wide temperature range, (iv) total unified recombination cross sections and velocity averaged recombination rate coefficients as functions of the photoelectron energy for comparison with experiments.

The present data are expected to be of high accuracy of about 10-15% based on (i) the very good agreement, less than 1%, of the energies with the experimental values, (ii) inclusion of important atomic effects such as relativistic effects, radiation damping of resonances, channel couplings, (iii) accuracy of the method from benchmarking with a number of experiments for photoionization (e.g., Nahar 2004) and electron-ion recombination (e.g., Zhang et al. 1999, Pradhan et al. 2001), and good agreement of the present results with existing rates. The present data are more than sufficient for extrapolation to high- $n, \ell$  necessary to account for all recombination cascade contributions. The unified method provides self-consistent atomic parameters for the inverse processes and hence more accurate analysis of X-ray and UV spectroscopy of laboratory and astrophysical sources.

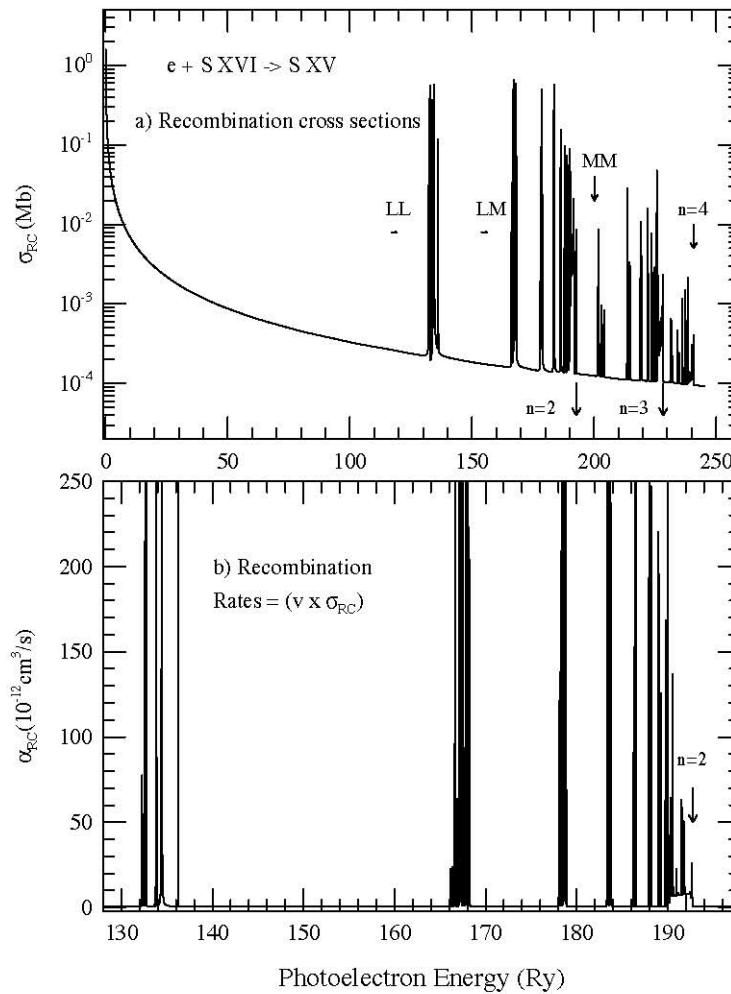


**Figure 9.** (a) Total unified ( $e + \text{ion}$ ) recombination cross sections,  $\sigma_{RC}$  and (b) unified recombination rate coefficients,  $\alpha_{RC}(E)$  with photoelectron energy for ( $e + \text{S XVI} \rightarrow \text{S XV}$ ). The separated resonance complexes, LL, LM, etc of  $n = 2$  and MM, MN etc. of  $n = 3$  and those of  $n = 4$  thresholds can be noted in (a). Detailed  $\alpha_{RC}(E)$  in (b) is given in energy range of experimental interest.

All photoionization and recombination data will be available on-line via webpage Nahar\_OSU\_RadiativeAtomicData(NORAD) at [www.astronomy.ohio-state.edu/~nahar/nahar\\_radiativeatomicdata](http://www.astronomy.ohio-state.edu/~nahar/nahar_radiativeatomicdata)

#### Acknowledgments

This work was supported partially by the NASA Astronomy and Physics Research and Analysis program. The computational work was carried out at the Ohio Supercomputer Center in Columbus, Ohio.



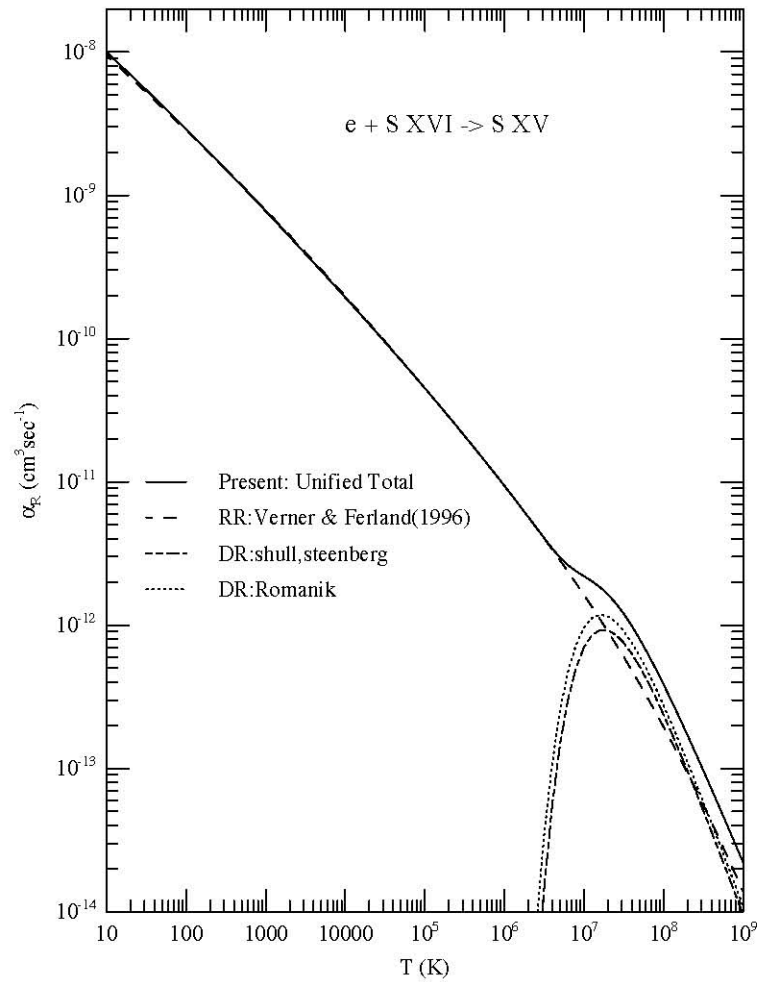


**Figure 10.** Total unified recombination rate coefficients  $\alpha_R(T)$  (solid curve) for S XV. The RR rates are by Verner & Ferland (1996) (dash), the DR rates are by Romanik (1988) (dot) and by Shull and Steenberg (1982, dot and dash).

## References

- [1] Bell, R.H. & Seaton, M.J. 1985, *J. Phys. B* 18, 1589
- [2] Berrington, K. A., Burke, P.G., Butler, K., Seaton, M.J., Storey, P.J., Taylor, K.T. & Yu Yan 1987, *J. Phys. B* 20, 6379
- [3] Berrington, K.A., Eissner, W., Norrington, P.H. 1995, *Comput. Phys. Commun.* 92, 290
- [4] Brinkman, A.C. et al., 2002, *A&A* 396, 761
- [5] Eissner, W., Jones, M., & Nussbaumer, H. 1974, *Comput. Phys. Commun.* 8, 270
- [6] Fernley, A., Taylor, K.T., & Seaton, M.J., 1987, *J. Phys. B*, 20, 6457
- [7] Hummer, D.G., Berrington, K.A., Eissner, W., Pradhan, A.K., Saraph, H.E., & Tully, J.A. 1993, *Astron. Astrophys.* 279, 298

- [8] Liedahl, D.A. & Paerls, F. 1996, ApJ 486, L33
- [9] Marshall, H.L., Claude R. Canizares, & Norbert S. Schulz, 2002, ApJ 564, 941-952
- [10] Nahar, S.N. 1996, Phys. Rev. A 53, 2417
- [11] Nahar, S.N. 2002, Astron. Astrophys. 389, 716
- [12] Nahar, S.N. 2004, Phys. Rev. A 69, 042714-1
- [13] Nahar, S.N. 2005, Astrophys. J. Suppl. 158, 80
- [14] Nahar, S.N. & Pradhan, A.K. 1992, Phys. Rev. Lett. 68, 1488
- [15] Nahar, S.N. & Pradhan, A.K. 1994, Phys. Rev. A 49, 1816
- [16] Nahar, S.N. & Pradhan, A.K. 2000, Phys. Scr. 61, 675
- [17] Nahar, S.N. & Pradhan, A.K. 2006, Phys. Rev. A 73, 062718-1
- [18] NIST compiled database, [www.nist.gov](http://www.nist.gov)
- [19] Oelgoetz, J. & Pradhan, A.K. 2001, MNRAS 327, L42
- [20] Oelgoetz, J. & Pradhan, A.K. 2004, MNRAS 354, 1093
- [21] Peach, G., Saraph, H.E., & Seaton, M.J., 1988, J. Phys. B, 21, 3669
- [22] Pradhan, A.K., Chen, Guo Xin, Nahar, S.N., and Zhang, H. L. 2001, Phys. Rev. Lett. 87, 183201
- [23] Pradhan, A.K. and Zhang, H. L. 1997, J. Phys. B 30, L571
- [24] Reeves, J.N. et al. 2002, Nature 416 512
- [25] Romanik, C. 1988, ApJ 330, 1022
- [26] Sakimoto, K., Terao, M., & Berrington, K.A. 1990, Phys. Rev. A 42, 291
- [27] Schippers, S., A. Müller, G. Gwinner, J. Linkemann, A. Saghiri and A. Wolf, ApJS 555, 1027 (2001)
- [28] Scott, N.S. & Burke, P.G. 1980, J. Phys. B 12, 4299
- [29] Scott, N.S. & Taylor, K.T. 1982, Comput. Phys. Commun. 25, 347
- [30] Shull, J.M. & van Steenberg, M. 1982, ApJS 48, 95 (values are fitted from the works of Jacobs et al as referenced in their papers)
- [31] Verner, D.A. & Ferland G. 1996, ApJS, 103, 467
- [32] Zhang, H.L., Nahar, S.N. & Pradhan, A.K. 1999, J. Phys. B, 32. 1459